Journal of Zhejiang University-SCIENCE A (Applied Physics & Engineering)
ISSN 1673-565X (Print); ISSN 1862-1775 (Online)
www.jzus.zju.edu.cn; www.springerlink.com
E-mail: jzus@zju.edu.cn

A coupled thermal–hydraulic–mechanical–chemical (THMC) model for methane hydrate bearing sediments using COMSOL Multiphysics*

Xiang SUN[1,3], Hao LUO‡[2,3], Kenichi SOGA‡[3]

[1]*Key Laboratory of Ocean Energy Utilization and Energy Conservation of Ministry of Education, Dalian University of Technology, Dalian 116024, China*

[2]*University of Cambridge, Cambridge CB21PZ, UK*

[3]*University of California, Berkeley, Berkeley CA 94720, USA*

E-mail: shyaansun@outlook.com; hl423@cam.ac.uk; soga@berkeley.edu

Received Aug. 30, 2017; Revision accepted Mar. 22, 2018; Crosschecked July 9, 2018

Abstract: Methane gas extraction by a deep well installed in methane hydrate bearing sediments (MHBS) found in deep subsea and permafrost regions is a coupled thermal–hydraulic–mechanical–chemical (THMC) process. The key processes include heat convection between layers, local deformation due to compaction, and stress relaxation caused by damage of the bonded structure. As improper production may induce formation compaction, sand production, and wellbore failures, a numerical code is needed to simulate the THMC processes during methane gas production so that geomechanics and production risks can be quantified. In this study, a nonlinear THMC model was implemented in the partial differential equations (PDE) and structural mechanics module of the COMSOL Multiphysics® finite element code. This paper describes the non-linear coupled governing equations of the mechanical behavior during hydrate dissociation. In particular, it introduces a new thermodynamics-based constitutive model to simulate the mechanical behavior of hydrate bearing sediments. The performance of the newly developed code was examined by comparing the computed results with test data and other simulation results. The differences between fully coupled and semi-coupled models were analyzed. For example, heterogeneous turbidite layers observed in the Nankai Trough were modeled, and behaviors such as heat convection between different layers, shear stress and strain concentration were examined.

Key words: Hydrate bearing sediments; Coupled thermal–hydraulic–mechanical–chemical (THMC) model; COMSOL; Gas production

https://doi.org/10.1631/jzus.A1700464 **CLC number:** TV5

1 Introduction

Methane hydrate, a form of clean energy also called “combustible ice”, has drawn global interest as an alternative energy resource to traditional fossil fuels (Zhao et al., 2011; Song et al., 2013; Yang et al., 2014). Currently, trials of hydrate gas production are conducted using gas recovery methods of depressurization, heat injection and/or chemical inhibition, during which hydrate dissociates and generates methane gas and water (Ruppel, 2011; Zhao et al., 2013, 2014, 2015; Song et al., 2015). The mechanical behavior of methane hydrate bearing sediment (MHBS) changes during the process of hydrate dissociation, which may induce catastrophic failures including layer collapse (Hannegan et al., 2004), sliding

‡ Corresponding author

* Project supported by the Key Program of National Natural Science Foundation of China (No. 51436003), the National Key Research and Development Program of China (Nos. 2017YFC0307305, 2016YFC0304001, and 2017YFC0307705), and the National Natural Science Foundation of China (Nos. 51676024 and 51509032)

ORCID: Xiang SUN, https://orcid.org/0000-0003-1060-5890

(McIver, 1982; Kayen and Lee, 1993; Paull et al., 2007), and damage to infrastructure (Borowski and Paul, 1997). Hyodo et al. (2014) studied the shear strength and deformation behavior of MHBS during hydrate decomposition by depressurization and heating. Song et al. (2010) and Li et al. (2016a, 2016b) studied the effect of temperature, confining pressure, strain rate, and mining methods on the shear or creep properties of MHBS, which are valuable for assessing the stability of the MHBS layer during hydrate production. However, few studies have focused on the effect of gas production on the mechanical behavior of the MHBS layer. It is important to build a coupled thermal–hydraulic–mechanical–chemical (THMC) model to investigate the influence of gas production on the mechanical behavior of the MHBS layer.

Many numerical coupled THMC models for MHBS have been proposed to simulate the mechanical behavior of MHBS during methane gas production (Ahmadi et al., 2004; Moridis et al., 2004; Kimoto et al., 2007; Kowalsky and Moridis, 2007; Klar et al., 2010; Kakumoto et al., 2011b; Kim et al., 2012; Uchida et al., 2016b). Uchida (2013) reported that the impacts of the mechanical behavior of hydrate bearing sediment include stress relaxation and soil compaction due to hydrate dissociation, softening, and dilatant behavior during shearing. Most models are based on the finite differential method (FDM) or finite volume method (FVM). Few models for MHBS are based on the finite element method (FEM) even though FEM is very robust for nonlinear deformation and stress calculations. COMSOL provides a user-friendly graphical user interface (GUI) that allows researchers to build and modify the model easily. This function is beneficial for improving the efficiency of modeling and for quickly testing different hypotheses.

The coupling system of the problem examined in this study consists of governing equations and auxiliary equations. The governing equations include the conservation of energy, mass, and momentum. All these equations are derived from the local balance conditions. As MHBS is a four-phase four-component composite, conservation equations should be built for each component. Because of the complexity of the problem, some simplifications may be needed to ensure the efficiency of the code. For example, chemical kinetics is used to describe hydrate dissociation. Auxiliary relationships, such as the van Genuchten unsaturated soil seepage model, thermodynamics-based constitutive model, and Biot's effective stress principle for unsaturated soil, are used to describe the methane hydrate gas production system in a relatively accurate way.

In this study, we used COMSOL to simulate the behavior of MHBS during gas production. A coupled THMC model was built upon the partial differential equations (PDE) module and structure mechanical module. A new feature called external material interface in COMSOL 5.3 was used to develop a thermodynamics-based methane hydrate constitutive model (TMH) for MHBS. Several comparisons with the models offered by other researchers were conducted to validate this model. Triaxial test data were used to validate the constitutive model. The difference between a fully coupled THMC model and a semi-coupled THMC model was discussed. Finally, we investigated the behavior of an MHBS turbidite layer during depressurization using the fully coupled THMC model.

2 Fully coupled THMC formulation

2.1 Definition of saturation

Mixture theory assumes that the behavior of a mixture is a combination of the behavior of each component and the interaction between these components. A component fraction is introduced to distinguish them. In mixture theory, the volume ratio, which is the ratio of component volume to mixture volume, tends to be used as the fraction:

$$n_\alpha = \frac{V_\alpha}{V}, \quad \alpha = \mathrm{s, w, g, h}, \tag{1}$$

where V is the bulk volume of each component, and α stands for soil (s), water (w), gas (g), or hydrate (h).

Hydrate saturation is defined by $s_h=n_h/n$, where n is the volume ratio of the void in host sediments or porosity. The rest of the void is filled with water, gas, and hydrate following a similar definition, i.e. water saturation $s_w=n_w/n$, gas saturation $s_g=n_g/n$, and flow saturation $s_f=s_w+s_g=n_w/n+n_g/n=n_f/n$. $n_f=1-n_s-n_h$.

Thus, the sum of hydrate, water, and gas saturation equals 1:

$$s_{\mathrm{w}}+s_{\mathrm{h}}+s_{\mathrm{g}}=1, \tag{2}$$

and the following equation can be derived:

$$\frac{\mathrm{d}s_{\mathrm{w}}}{\mathrm{d}t}+\frac{\mathrm{d}s_{\mathrm{g}}}{\mathrm{d}t}+\frac{\mathrm{d}s_{\mathrm{h}}}{\mathrm{d}t}=0. \tag{3}$$

2.2 Methane hydrate dissociation

As suggested by Kim et al. (1987), the first-order kinetics were used as the governing equation for the dissociation process of hydrate; the rate of dissociation is proportional to the product of the specific surface area and the fugacity difference:

$$R_{\mathrm{h}}=n\left(s_{\mathrm{h}}A_{\mathrm{hs}}K_{\mathrm{d}}\left\langle f_{\mathrm{eq}}-f_{\mathrm{g}}\right\rangle\right), \tag{4}$$

where R_{h} is the rate of hydrate phase change expressed in hydrate moles, K_{d} is the hydrate dissociation dynamics constant, A_{hs} is the hydrate surface area for unit volume of hydrate, f_{g} is the gas pressure at a certain temperature, f_{eq} is the phase equilibrium pressure dependent on this temperature, and $\langle\ \rangle$ are Macaulay brackets describing the ramp function.

The phase equilibrium curve shows the conditions of temperature and pressure for hydrate dissociation. At a certain temperature T, methane hydrate forms when the pressure is higher than the equilibrium pressure. On the other hand, methane hydrate dissociates when the pressure is lower than the equilibrium pressure. The phase equilibrium pressure p_{eq} can be obtained using a Kamath regression equation (Kamath, 1998):

$$p_{\mathrm{eq}}=\exp\left(e_1-\frac{e_2}{T}\right), \tag{5}$$

where e_1 and e_2 are two regression coefficients. In this research, the two coefficients were e_1=39.08 and e_2=8533 based on Kim et al. (1987).

According to Kim et al. (1987), the hydrate dissociation constant K_{d} is dependent on the surface activation energy and temperature:

$$K_{\mathrm{d}}=K_{\mathrm{d0}}\exp\left(\frac{\Delta E_{\mathrm{d}}}{RT}\right), \tag{6}$$

where ΔE_{d}=−78300 J/mol is the surface activation energy of hydrate dissociation, K_{d0}=1.24×10^5 mol/(m^2·Pa·s), and R is the ideal gas constant.

2.3 Mass conservation equations

In porous media mechanics, the differential form of mass conservation equation can be written as

$$\frac{\mathrm{d}(\rho_\alpha n_\alpha)}{\mathrm{d}t}+\rho_\alpha n_\alpha\nabla\cdot\boldsymbol{v}_\alpha=\frac{\mathrm{d}m_\alpha}{\mathrm{d}t}, \tag{7}$$

where ρ_α is the density of material α, $\mathrm{d}m_\alpha/\mathrm{d}t$ is the increment of the mass of material α, and $\boldsymbol{v}_\alpha$ is the velocity of material α. The mass conservation equations for soil, hydrate, gas, and water can be obtained using the above equation.

For soils (s), the mass conservation equation derived by chain rule, ignoring the influence of pressure and temperature on the density of soil, is given as

$$-\frac{1}{1-n}\frac{\mathrm{d}n}{\mathrm{d}t}+\nabla\cdot\boldsymbol{v}_{\mathrm{s}}=0. \tag{8}$$

If the soil is considered as the skeleton, i.e. deformable but immobile, the following equation can be used:

$$\nabla\cdot\boldsymbol{v}_{\mathrm{s}}=\mathrm{d}\varepsilon_{\mathrm{v}}/\mathrm{d}t, \tag{9}$$

where ε_{v} is the volumetric strain of the soil skeleton. The mass conservation equations for methane gas (g) and water (w) can be derived using the following expressions:

$$n\frac{\mathrm{d}s_{\mathrm{w}}}{\mathrm{d}t}+s_{\mathrm{w}}\frac{\mathrm{d}n}{\mathrm{d}t}+\frac{n_{\mathrm{w}}}{\rho_{\mathrm{w}}}\frac{\mathrm{d}\rho_{\mathrm{w}}}{\mathrm{d}t}+n_{\mathrm{w}}\nabla\cdot\boldsymbol{v}_{\mathrm{w}}=\frac{1}{\rho_{\mathrm{w}}}\frac{\mathrm{d}m_{\mathrm{w}}}{\mathrm{d}t}, \tag{10}$$

$$n\frac{\mathrm{d}s_{\mathrm{g}}}{\mathrm{d}t}+s_{\mathrm{g}}\frac{\mathrm{d}n}{\mathrm{d}t}+\frac{n_{\mathrm{g}}}{\rho_{\mathrm{g}}}\frac{\mathrm{d}\rho_{\mathrm{g}}}{\mathrm{d}t}+n_{\mathrm{g}}\nabla\cdot\boldsymbol{v}_{\mathrm{g}}=\frac{1}{\rho_{\mathrm{g}}}\frac{\mathrm{d}m_{\mathrm{g}}}{\mathrm{d}t}, \tag{11}$$

and for methane hydrate (h), the mass conservation equation is

$$n\frac{\mathrm{d}s_\mathrm{h}}{\mathrm{d}t}+s_\mathrm{h}\frac{\mathrm{d}n}{\mathrm{d}t}+\frac{n_\mathrm{h}}{\rho_\mathrm{h}}\frac{\mathrm{d}\rho_\mathrm{h}}{\mathrm{d}t}+n_\mathrm{h}\nabla\cdot\boldsymbol{v}_\mathrm{h}=\frac{1}{\rho_\mathrm{h}}\frac{\mathrm{d}m_\mathrm{h}}{\mathrm{d}t}. \tag{12}$$

As the skeleton is formed by both soil and hydrate, we assumed that the hydrate is also dissociable and deformable, but there is no relative motion to the soil, so v_s=v_h (Kimoto et al., 2007).

The water and gas continuum equations can be converted into Eqs. (13) and (14), respectively, by substituting Darcy velocity into them and ignoring the influence of the spatial distribution of n_w and n_g on mass balance:

$$n\frac{\mathrm{d}s_\mathrm{w}}{\mathrm{d}t}+s_\mathrm{w}\frac{\mathrm{d}\varepsilon_\mathrm{v}}{\mathrm{d}t}+\frac{n_\mathrm{w}}{\rho_\mathrm{w}}\frac{\mathrm{d}\rho_\mathrm{w}}{\mathrm{d}t}+\nabla\cdot\boldsymbol{q}_\mathrm{w}=\frac{1}{\rho_\mathrm{w}}\frac{\mathrm{d}m_\mathrm{w}}{\mathrm{d}t}, \tag{13}$$

$$n\frac{\mathrm{d}s_\mathrm{g}}{\mathrm{d}t}+s_\mathrm{g}\frac{\mathrm{d}\varepsilon_\mathrm{v}}{\mathrm{d}t}+\frac{n_\mathrm{g}}{\rho_\mathrm{g}}\frac{\mathrm{d}\rho_\mathrm{g}}{\mathrm{d}t}+\nabla\cdot\boldsymbol{q}_\mathrm{g}=\frac{1}{\rho_\mathrm{g}}\frac{\mathrm{d}m_\mathrm{g}}{\mathrm{d}t}, \tag{14}$$

where $\boldsymbol{q}_\mathrm{w}$=$n_\mathrm{w}$($\boldsymbol{v}_\mathrm{w}$−$\boldsymbol{v}_\mathrm{s}$) and $\boldsymbol{q}_\mathrm{g}$=$n_\mathrm{g}$($\boldsymbol{v}_\mathrm{g}$−$\boldsymbol{v}_\mathrm{s}$). The chemical reaction equation of hydrate dissociation is

$$\mathrm{CH_4\cdot 6H_2O}\rightarrow\mathrm{CH_4+6H_2O}. \tag{15}$$

The dissociation rates for hydrate, water, and gas are defined as

$$\frac{\mathrm{d}m_\mathrm{h}}{\mathrm{d}t}=-M_\mathrm{h}R_\mathrm{h}, \tag{16}$$

$$\frac{\mathrm{d}m_\mathrm{w}}{\mathrm{d}t}=6M_\mathrm{w}R_\mathrm{h}, \tag{17}$$

$$\frac{\mathrm{d}m_\mathrm{g}}{\mathrm{d}t}=M_\mathrm{g}R_\mathrm{h}, \tag{18}$$

where M_h, M_w, and M_g are respectively the molar masses of hydrate, water, and gas in a relation of

$$\frac{\mathrm{d}m_\mathrm{g}}{\mathrm{d}t}+\frac{\mathrm{d}m_\mathrm{w}}{\mathrm{d}t}+\frac{\mathrm{d}m_\mathrm{h}}{\mathrm{d}t}=0. \tag{19}$$

2.4 Momentum conservation equations

According to mixture theory, the momentum conservation equations for α component can be written as a Navier-Stokes form:

$$\begin{aligned}&n_\alpha\rho_\alpha\frac{\mathrm{d}\boldsymbol{v}_\alpha}{\mathrm{d}t}+n_\alpha\rho_\alpha\boldsymbol{v}_\alpha\cdot\nabla\boldsymbol{v}_\alpha\\&=\nabla\cdot(n_\alpha\boldsymbol{\sigma}_\alpha)+\boldsymbol{F}_\alpha-\frac{\mathrm{d}m_\alpha}{\mathrm{d}t}\boldsymbol{v}_\alpha+n_\alpha\rho_\alpha\boldsymbol{g}_\alpha=0,\end{aligned} \tag{20}$$

where $\boldsymbol{\sigma}_\alpha$ is the stress of phase α, $\boldsymbol{F}_\alpha$ is the interaction between different phases such as seepage force, and $\boldsymbol{g}$ is the acceleration of gravity. It is difficult to solve the equations above because they contain four Navier-Stokes equations which are highly nonlinear. Therefore, it is necessary to simplify them using the following assumptions: (1) The inertia and convection terms can be ignored because the velocities of fluids are relatively slow; (2) The Biot effective stress principle for unsaturated soil is feasible in this particular problem; (3) The interactions between different phases are not the key factor, except between the water and gas seepage forces; (4) The momentum changes due to phase changes are not taken into account. Based on these assumptions, the following force balance equations can be obtained:

$$\nabla\cdot(\boldsymbol{\sigma}'-p_\mathrm{p}\boldsymbol{\delta})+(n_\mathrm{s}\rho_\mathrm{s}+n_\mathrm{w}\rho_\mathrm{w}+n_\mathrm{g}\rho_\mathrm{g}+n_\mathrm{h}\rho_\mathrm{h})\boldsymbol{g}=0, \tag{21}$$

$$\nabla p_\mathrm{w}+\frac{\mu_\mathrm{w}}{\boldsymbol{K}_\mathrm{h}k_\mathrm{w}}\boldsymbol{q}_\mathrm{w}=\rho_\mathrm{w}\boldsymbol{g}, \tag{22}$$

$$\nabla p_\mathrm{g}+\frac{\mu_\mathrm{g}}{\boldsymbol{K}_\mathrm{h}k_\mathrm{g}}\boldsymbol{q}_\mathrm{g}=\rho_\mathrm{g}\boldsymbol{g}, \tag{23}$$

where $\boldsymbol{\delta}$ is unit matrix; p_p is the pore pressure; μ_w and μ_g are the dynamic viscosities of water and gas; p_w and p_g are the pressures of water and gas, respectively; $\boldsymbol{\sigma}'$ is the effective stress governing deformation and is related to hydrate saturation when sediments bear hydrates; $\boldsymbol{K}_\mathrm{h}$ is the intrinsic permeability tensor of the hydrate formation. Based on Bishop's assumption (Bishop, 1959) and the following experimental calibration (Schrefler, 1984; Jommi and di Prisco, 1994; Gens, 1996; Khalili and Khabbaz, 1998), the average pore pressure can be defined as

$$p_\mathrm{p}=\frac{s_\mathrm{w}p_\mathrm{w}+s_\mathrm{g}p_\mathrm{g}}{s_\mathrm{w}+s_\mathrm{g}}. \tag{24}$$

With hydrate dissociation, more pore space becomes available for fluid flow and hence the permeability for

hydrate-bearing sediment increases following the expression of Minagawa et al. (2008), combined with the power type empirical formula (Taylor, 1948).

The state equations taking into consideration the fluid density change influenced by the change of pressure and temperature are as follows:

$$\frac{1}{\rho_w}\frac{\mathrm{d}\rho_w}{\mathrm{d}t}=\frac{1}{B_w}\frac{\mathrm{d}p_w}{\mathrm{d}t}-\beta_w\frac{\mathrm{d}T}{\mathrm{d}t}, \tag{25}$$

$$\frac{1}{\rho_g}\frac{\mathrm{d}\rho_g}{\mathrm{d}t}=\frac{1}{B_g}\frac{\mathrm{d}p_g}{\mathrm{d}t}-\beta_g\frac{\mathrm{d}T}{\mathrm{d}t}, \tag{26}$$

where B_w and B_g are the bulk moduli of water and methane gas, and β_w and β_g are the thermal expansion coefficients of water and methane gas, respectively.

2.5 Energy conservation equations

For simplification, four phase energy balance terms are summarized in a single energy balance equation as a system with the dependent variable T by integrating all energy equations together and eliminating the interphase heat transfer fluxes. We assumed that the heat exchange in this system is conduction and convection. Heat convection here is heat transfer by the motion of fluid, defined as

$$\nabla\cdot(c_w\rho_w\boldsymbol{q}_wT)+\nabla\cdot(c_g\rho_g\boldsymbol{q}_gT), \tag{27}$$

where c_w and c_g are the specific heat of water and methane gas, respectively.

Heat conduction is

$$\nabla\cdot(-K_T\nabla T), \tag{29}$$

where K_T is the volumetric mean of the thermal conductivity, i.e.

$$K_T=n_sK_{Ts}+n_gK_{Tg}+n_hK_{Th}+n_wK_{Tw}, \tag{30}$$

where K_{Ts}, K_{Tw}, K_{Tg}, and K_{Th} are the thermal conductivity of soil, water, methane gas, and methane hydrate, respectively.

As hydrate dissociation is an endothermic process, temperature change due to hydrate dissociation is given by

$$\frac{\mathrm{d}Q_h}{\mathrm{d}t}=-\Delta HR_h, \tag{31}$$

where ΔH is the heat change due to the phase change of hydrate, which can be obtained by Kamath (1998) regression as

$$\Delta H=c_1+c_2T, \tag{32}$$

where c_1 and c_2 are regression coefficients, i.e. c_1= 56599, c_2=16.744.

The energy conservation equations of hydrate-bearing soil during dissociation can be described by multicomponent mixture theory. Because of the low velocity of fluid, the kinematic energy can be ignored in this problem. As the work input has little impact on the change of temperature, this part can be ignored as well. Hence, the energy balance can be expressed as

$$\begin{aligned}c_T\frac{\mathrm{d}T}{\mathrm{d}t}+\nabla\cdot\left(-K_T\nabla T\right)+\nabla\cdot\left(c_w\rho_w\boldsymbol{q}_wT\right)\\+\nabla\cdot\left(c_g\rho_g\boldsymbol{q}_gT\right)=-\Delta HR_h,\end{aligned} \tag{33}$$

where the heat capacity of the mixture $c_T=\rho_sn_sc_s+\rho_gn_gc_g+\rho_hn_hc_h+\rho_wn_wc_w$, and c_s and c_h are the specific heat of soil and methane hydrate, respectively.

2.6 van Genuchten model

In porous media, gas and water may be trapped inside pores as "residual gas" and "residual water". Therefore, the presence of hydrate in pores may affect the saturation of residual water and gas. The effective water saturation s_e is defined by the following equation without consideration of the presence of hydrate:

$$s_e=\frac{V_w-V_{wr}}{V_f-V_{wr}-V_{gr}}=\frac{s_w-s_{wr}}{1-s_{wr}-s_{gr}}, \tag{34}$$

where V_{wr} is the volume of residual water, V_{gr} is the volume of residual gas, V_f is the volume of fluid, V_v is the volume of void, and $V_f=V_w+V_g=V_v$. s_{wr} and s_{gr} are the saturations of residual water and gas, respectively. For hydrate-bearing soil, $V_f=V_w+V_g=V_v-V_h$, and hence the following equation can be obtained:

$$s_e=\frac{V_w/V_f-V_{wr}/V_f}{V_f/V_f-V_{wr}/V_f-V_{gr}/V_f}=\frac{\dfrac{s_w}{1-s_h}-s_{wr}}{1-s_{wr}-s_{gr}}, \tag{35}$$

where $s_{wr}=V_{wr}/V_f$, $s_{gr}=V_{gr}/V_f$, $s_w=V_w/V_v$, $s_h=V_h/V_v$. Note that,

$$s_g=s_{gr}(1-s_h)\le s_{gr},\quad s_e=1, \tag{36}$$

$$s_w=s_{wr}(1-s_h)\le s_{wr},\quad s_e=0. \tag{37}$$

In this simulation, the residual gas saturation s_{gr} was calculated by

$$s_{gr}=s_{gr0}\{1-[s_g/(1-s_{wr})-1]^2\}, \tag{38}$$

where s_{gr0} is the maximum residual gas saturation obtained in the state where all of the available pore space is filled with gas (i.e. $s_g=1-s_{wr}$).

k_w and k_g are the relative permeability coefficients of water and gas, respectively:

$$k_w=s_e^{n_2}\left[1-(1-s_e^{1/n_1})^{n_1}\right]^2, \tag{39}$$

$$k_g=(1-s_e)^{n_3}(1-s_e^{1/n_1})^{2n_1}, \tag{40}$$

where n_1, n_2, and n_3 are the van Genuchten parameters describing the soil-fluid characteristic curve. The difference between gas pressure and water pressure is defined as capillary pressure $p_c=p_g-p_w$ in the van Genuchten relationship (van Genuchten, 1980):

$$s_e=\left[(p_c/p_0)^{\frac{1}{1-n_1}}+1\right]^{-n_1}, \tag{41}$$

where p_0 is also the van Genuchten parameter describing the soil-fluid characteristic curve.

2.7 Thermodynamics-based constitutive model for MHBS

A constitutive model is required to build the relationship between effective stress σ' and strain ε of the solid skeleton. The elasto-plastic critical state model used in this study consists of four formulations including an elasticity part, dilatancy rule, hardening rule, and yield function. Uchida et al. (2012) extended the critical state model to describe the mechanical behavior of MHBS by introducing hydrate saturation into these four formulations. Sun et al. (2015) further developed this model based on thermodynamics to have a non-associated flow rule, and considered the influence of the shape of yield loci on stress-strain relationship prediction.

In the thermodynamics-based constitutive model, the yield function f can be expressed as

$$f=\frac{(p'-\rho')^2}{A^2}+\frac{q^2}{B^2}-1=0, \tag{42}$$

and the dilatancy function, which is defined as a ratio of the volumetric plastic strain increment to the equivalent plastic strain increment, is expressed as

$$D=\frac{\mathrm{d}\varepsilon_v^p}{\mathrm{d}\varepsilon_s^p}=\frac{(p'-\rho')B^2}{qA^2}, \tag{43}$$

where

$$A=(1-\gamma)p'+\frac{1}{2}\gamma(p'_{cd}+p'_{cs})+p'_{cc}, \tag{44}$$

$$B=(1-\alpha)Mp'+\alpha M\rho'+Mp'_{cc}, \tag{45}$$

$$\rho'=\frac{1}{2}\gamma(p'_{cc}+p'_{cd}+p'_{cs})-\left(1-\frac{\gamma}{2}\right)p'_{cc}, \tag{46}$$

$$p'=\mathrm{trace}(\boldsymbol{\sigma}'), \tag{47}$$

$$q=\sqrt{\frac{3}{2}(\boldsymbol{\sigma}'-p'\boldsymbol{\delta})^2}. \tag{48}$$

R, p'_{cc}, p'_{cd}, and p'_{cs} are the hardening parameters. M is the slope of the critical state line. α and γ are material parameters governing the shape of the yield surface. The hardening rule can be described as

$$\mathrm{d}p'_{cs}=\frac{\nu p'_{cs}}{\lambda-\kappa}\mathrm{d}\varepsilon_v^p, \tag{49}$$

$$p'_{cc}=c\left(s_h^{mec}\right)^d, \tag{50}$$

$$p'_{cd}=a\left(s_h^{mec}\right)^b, \tag{51}$$

$$\mathrm{d}R=-u\ln R\left|\mathrm{d}\boldsymbol{\varepsilon}^p\right|, \tag{52}$$

where

$$s_{\mathrm{h}}^{\mathrm{mec}} = \chi s_{\mathrm{h}}, \tag{53}$$

$$\chi = \chi_0 \exp(-m\varepsilon_{\mathrm{s}}^{\mathrm{p}}), \tag{54}$$

u, m, a, b, c, d, λ, κ, χ_0 and v are the material parameters related to the hardening, softening, and debonding behavior of soils, and $\boldsymbol{\varepsilon}^{\mathrm{p}}$ is the plastic strain tensor.

The elastic shear modulus is expressed as

$$G = \frac{3K(1-2\mu)}{2(1+\mu)} + m_2 s_{\mathrm{h}}^{\mathrm{mec}}, \tag{55}$$

where $K = \dfrac{\nu p'}{\kappa}$, μ, ν, and m_2 are the parameters which describe the elastic behavior.

The stress-strain relationship can be written as

$$\begin{aligned}
\mathrm{d}\boldsymbol{\sigma}' = & \left(\boldsymbol{E}^{\mathrm{e}} - \frac{\boldsymbol{E}^{\mathrm{e}} : \boldsymbol{d} \otimes \dfrac{\partial f}{\partial \boldsymbol{\sigma}'} : \boldsymbol{E}^{\mathrm{e}}}{\dfrac{\partial f}{\partial \boldsymbol{\sigma}'} : \boldsymbol{E}^{\mathrm{e}} : \boldsymbol{d} + H} \right) : \mathrm{d}\boldsymbol{\varepsilon} \\
& + \left\{ \left[\chi \boldsymbol{E}^{\mathrm{h}} : \boldsymbol{\varepsilon}^{\mathrm{e}} - \boldsymbol{E}^{\mathrm{e}} : \boldsymbol{d} \left(\frac{\partial f}{\partial p'_{\mathrm{cc}}} cd (s_{\mathrm{h}}^{\mathrm{mec}})^{d-1} \right.\right.\right. \\
& \left.\left.\left. + \frac{\partial f}{\partial p'_{\mathrm{cd}}} ab (s_{\mathrm{h}}^{\mathrm{mec}})^{b-1} \right] \chi \middle/ \left(\frac{\partial f}{\partial \boldsymbol{\sigma}'} : \boldsymbol{E}^{\mathrm{e}} : \boldsymbol{d} + H \right) \right\} \mathrm{d}s_{\mathrm{h}} \\
& + \left(\frac{\mathrm{d}\boldsymbol{\sigma}'}{\mathrm{d}T} - \frac{\boldsymbol{E}^{\mathrm{e}} : \boldsymbol{d} \dfrac{\partial f}{\partial \boldsymbol{\sigma}'} \dfrac{\partial \boldsymbol{\sigma}'}{\partial T}}{\dfrac{\partial f}{\partial \boldsymbol{\sigma}'} : \boldsymbol{E}^{\mathrm{e}} : \boldsymbol{d} + H} \right) \mathrm{d}T,
\end{aligned} \tag{56}$$

where

$$\begin{aligned}
H = & \frac{\partial f}{\partial p'_{\mathrm{cc}}} dm p'_{\mathrm{cc}} + \frac{\partial f}{\partial p'_{\mathrm{cd}}} bm p'_{\mathrm{cd}} \\
& - \frac{\partial f}{\partial p'_{\mathrm{cs}}} \frac{\nu p'_{\mathrm{cs}}}{\lambda - \kappa} D + \frac{\partial f}{\partial R} u \ln R |\boldsymbol{d}|, \\
\boldsymbol{d} = & D \frac{\partial p'}{\partial \boldsymbol{\sigma}'} + \frac{\partial q}{\partial \boldsymbol{\sigma}'},
\end{aligned}$$

where $\boldsymbol{E}^{\mathrm{e}}$ is the elastic matrix, and $\boldsymbol{E}^{\mathrm{h}}$ is the elastic matrix related to hydrate saturation. The physical meaning of all these parameters and the advantages of this model have been given by Uchida et al. (2012, 2016a) and Sun et al. (2015).

3 COMSOL implementation

To build the coupled THMC model in COMSOL 5.3, the form of the equations above needed to be rearranged to meet the requirements of COMSOL. In this implementation, the primary dependent variables are displacement $\boldsymbol{u}$, p_{w}, p_{g}, and T, and the governing equation system consists of the following four equations with divergence terms.

1. Force balance equation

$$\boldsymbol{f} = \nabla \cdot \left(-\boldsymbol{D} : (\boldsymbol{L} : \boldsymbol{u} - \boldsymbol{\varepsilon}^{\mathrm{p}}) + \frac{s_{\mathrm{w}} p_{\mathrm{w}} + s_{\mathrm{g}} p_{\mathrm{g}}}{s_{\mathrm{w}} + s_{\mathrm{g}}} \boldsymbol{\delta} \right), \tag{57}$$

where $\boldsymbol{D}$ is the elastic matrix, and $\boldsymbol{L}$ is the derivative operator.

2. Mass balance of water flow

$$\begin{aligned}
& \left(\frac{n_{\mathrm{w}}}{B_{\mathrm{w}}} - n \frac{\partial s_{\mathrm{w}}}{\partial s_{\mathrm{e}}} \frac{\mathrm{d}s_{\mathrm{e}}}{\mathrm{d}p_{\mathrm{c}}} \right) \frac{\mathrm{d}p_{\mathrm{w}}}{\mathrm{d}t} \\
& \quad + \nabla \cdot \left(-\frac{K_{\mathrm{h}} k_{\mathrm{w}}}{\mu_{\mathrm{w}}} \left(\nabla p_{\mathrm{w}} - \rho_{\mathrm{w}} \boldsymbol{g} \right) \right) \\
& \quad = \left(6 \frac{1}{\rho_{\mathrm{w}}} M_{\mathrm{w}} + \frac{1}{\rho_{\mathrm{h}}} \frac{\partial s_{\mathrm{w}}}{\partial s_{\mathrm{h}}} M_{\mathrm{h}} \right) R_{\mathrm{h}} \\
& \quad - n \frac{\partial s_{\mathrm{w}}}{\partial s_{\mathrm{e}}} \frac{\mathrm{d}s_{\mathrm{e}}}{\mathrm{d}p_{\mathrm{c}}} \frac{\mathrm{d}p_{\mathrm{g}}}{\mathrm{d}t} + \left(s_{\mathrm{h}} \frac{\partial s_{\mathrm{w}}}{\partial s_{\mathrm{h}}} - s_{\mathrm{w}} \right) \boldsymbol{\delta} : \boldsymbol{L} : \frac{\mathrm{d}\boldsymbol{u}}{\mathrm{d}t} \\
& \quad + \left(n_{\mathrm{w}} \beta_{\mathrm{w}} - n_{\mathrm{h}} \beta_{\mathrm{h}} \frac{\partial s_{\mathrm{w}}}{\partial s_{\mathrm{h}}} \right) \frac{\mathrm{d}T}{\mathrm{d}t}.
\end{aligned} \tag{58}$$

3. Mass balance of gas flow

$$\begin{aligned}
& \left(\frac{n_{\mathrm{g}}}{B_{\mathrm{g}}} + n \frac{\partial s_{\mathrm{g}}}{\partial s_{\mathrm{e}}} \frac{\mathrm{d}s_{\mathrm{e}}}{\mathrm{d}p_{\mathrm{c}}} \right) \frac{\mathrm{d}p_{\mathrm{g}}}{\mathrm{d}t} \\
& \quad + \nabla \cdot \left(-\frac{K_{\mathrm{h}} k_{\mathrm{g}}}{\mu_{\mathrm{g}}} \left(\nabla p_{\mathrm{g}} - \rho_{\mathrm{g}} \boldsymbol{g} \right) \right) \\
& \quad = \left(\frac{1}{\rho_{\mathrm{g}}} M_{\mathrm{g}} + \frac{1}{\rho_{\mathrm{h}}} \frac{\partial s_{\mathrm{g}}}{\partial s_{\mathrm{h}}} M_{\mathrm{h}} \right) R_{\mathrm{h}} \\
& \quad + n \frac{\partial s_{\mathrm{g}}}{\partial s_{\mathrm{e}}} \frac{\mathrm{d}s_{\mathrm{e}}}{\mathrm{d}p_{\mathrm{c}}} \frac{\mathrm{d}p_{\mathrm{w}}}{\mathrm{d}t} + \left(s_{\mathrm{h}} \frac{\partial s_{\mathrm{g}}}{\partial s_{\mathrm{h}}} - s_{\mathrm{g}} \right) \boldsymbol{\delta} : \boldsymbol{L} : \frac{\mathrm{d}\boldsymbol{u}}{\mathrm{d}t} \\
& \quad + \left(n_{\mathrm{g}} \beta_{\mathrm{g}} - n_{\mathrm{g}} \beta_{\mathrm{h}} \frac{\partial s_{\mathrm{g}}}{\partial s_{\mathrm{h}}} \right) \frac{\mathrm{d}T}{\mathrm{d}t}.
\end{aligned} \tag{59}$$

4. Energy conservation

$$c_{\mathrm{T}}\frac{\mathrm{d}T}{\mathrm{d}t}+\nabla\cdot\left(-K_{\mathrm{T}}\nabla T\right)+\nabla\cdot\left(c_{\mathrm{w}}\rho_{\mathrm{w}}\boldsymbol{q}_{\mathrm{w}}T\right)+\nabla\cdot\left(c_{\mathrm{g}}\rho_{\mathrm{g}}\boldsymbol{q}_{\mathrm{g}}T\right)=-\Delta HR_{\mathrm{h}}. \tag{60}$$

The weak form of the governing equations is

$$\begin{aligned}&\int_{\Omega}\nabla\cdot\boldsymbol{W}_{\mathrm{u}}\cdot\left(\boldsymbol{D}:\left(\boldsymbol{L}:\boldsymbol{u}-\boldsymbol{\varepsilon}^{\mathrm{p}}\right)-\frac{s_{\mathrm{w}}p_{\mathrm{w}}+s_{\mathrm{g}}p_{\mathrm{g}}}{s_{\mathrm{w}}+s_{\mathrm{g}}}\boldsymbol{\delta}\right)\mathrm{d}V\\&\quad=\int_{\Omega}\boldsymbol{W}_{\mathrm{u}}\cdot\boldsymbol{f}\mathrm{d}V+\int_{\partial\Omega}\boldsymbol{W}_{\mathrm{u}}\cdot\boldsymbol{t}\mathrm{d}S,\end{aligned} \tag{61}$$

$$\begin{aligned}&\int_{\Omega}\nabla W_{\mathrm{pw}}\cdot\frac{K_{\mathrm{h}}k_{\mathrm{w}}}{\mu_{\mathrm{w}}}\left(\nabla p_{\mathrm{w}}-\rho_{\mathrm{w}}\boldsymbol{g}\right)\mathrm{d}V\\&\quad=\int_{\Omega}W_{\mathrm{pw}}\left[\left(6\frac{1}{\rho_{\mathrm{w}}}M_{\mathrm{w}}+\frac{1}{\rho_{\mathrm{h}}}\frac{\partial s_{\mathrm{w}}}{\partial s_{\mathrm{h}}}M_{\mathrm{h}}\right)R_{\mathrm{h}}\right.\\&\qquad-n\frac{\partial s_{\mathrm{w}}}{\partial s_{\mathrm{e}}}\frac{\mathrm{d}s_{\mathrm{e}}}{\mathrm{d}p_{\mathrm{c}}}\frac{\mathrm{d}p_{\mathrm{g}}}{\mathrm{d}t}\\&\qquad\left.+\left(n_{\mathrm{w}}\beta_{\mathrm{w}}-n_{\mathrm{h}}\beta_{\mathrm{h}}\frac{\partial s_{\mathrm{w}}}{\partial s_{\mathrm{h}}}\right)\frac{\mathrm{d}T}{\mathrm{d}t}\right]\mathrm{d}V\\&\qquad+\int_{\Omega}W_{\mathrm{pw}}\left[\left(s_{\mathrm{h}}\frac{\partial s_{\mathrm{w}}}{\partial s_{\mathrm{h}}}-s_{\mathrm{w}}\right)\boldsymbol{\delta}:\boldsymbol{L}:\frac{\mathrm{d}\boldsymbol{u}}{\mathrm{d}t}\right.\\&\qquad\left.-\left(\frac{n_{\mathrm{w}}}{B_{\mathrm{w}}}-n\frac{\partial s_{\mathrm{w}}}{\partial s_{\mathrm{e}}}\frac{\mathrm{d}s_{\mathrm{e}}}{\mathrm{d}p_{\mathrm{c}}}\right)\frac{\mathrm{d}p_{\mathrm{w}}}{\mathrm{d}t}\right]\mathrm{d}V\\&\qquad+\int_{\partial\Omega}W_{\mathrm{pw}}\boldsymbol{n}\cdot\boldsymbol{q}_{\mathrm{w}}\mathrm{d}S,\end{aligned} \tag{62}$$

$$\begin{aligned}&\int_{\Omega}\nabla W_{\mathrm{pg}}\cdot\frac{K_{\mathrm{h}}k_{\mathrm{g}}}{\mu_{\mathrm{g}}}\left(\nabla p_{\mathrm{g}}-\rho_{\mathrm{g}}\boldsymbol{g}\right)\mathrm{d}V\\&\quad=\int_{\Omega}W_{\mathrm{pg}}\left[\left(\frac{1}{\rho_{\mathrm{g}}}M_{\mathrm{g}}+\frac{1}{\rho_{\mathrm{h}}}\frac{\partial s_{\mathrm{g}}}{\partial s_{\mathrm{h}}}M_{\mathrm{h}}\right)R_{\mathrm{h}}\right.\\&\qquad+n\frac{\partial s_{\mathrm{g}}}{\partial s_{\mathrm{e}}}\frac{\mathrm{d}s_{\mathrm{e}}}{\mathrm{d}p_{\mathrm{c}}}\frac{\mathrm{d}p_{\mathrm{w}}}{\mathrm{d}t}+\left(n_{\mathrm{g}}\beta_{\mathrm{g}}-n_{\mathrm{h}}\beta_{\mathrm{h}}\frac{\partial s_{\mathrm{g}}}{\partial s_{\mathrm{h}}}\right)\frac{\mathrm{d}T}{\mathrm{d}t}\Bigg]\mathrm{d}V\\&\qquad+\int_{\Omega}W_{\mathrm{pg}}\left[\left(s_{\mathrm{h}}\frac{\partial s_{\mathrm{g}}}{\partial s_{\mathrm{h}}}-s_{\mathrm{g}}\right)\boldsymbol{\delta}:\boldsymbol{L}:\frac{\mathrm{d}\boldsymbol{u}}{\mathrm{d}t}\right.\\&\qquad\left.-\left(\frac{n_{\mathrm{g}}}{B_{\mathrm{g}}}+n\frac{\partial s_{\mathrm{g}}}{\partial s_{\mathrm{e}}}\frac{\mathrm{d}s_{\mathrm{e}}}{\mathrm{d}p_{\mathrm{c}}}\right)\frac{\mathrm{d}p_{\mathrm{g}}}{\mathrm{d}t}\right]\mathrm{d}V\\&\qquad+\int_{\partial\Omega}W_{\mathrm{pg}}\boldsymbol{n}\cdot\boldsymbol{q}_{\mathrm{g}}\mathrm{d}S,\end{aligned} \tag{63}$$

$$\begin{aligned}&\int_{\Omega}\nabla W_{\mathrm{T}}\cdot\left(K_{\mathrm{T}}\nabla T-c_{\mathrm{w}}\rho_{\mathrm{w}}\boldsymbol{q}_{\mathrm{w}}T-c_{\mathrm{g}}\rho_{\mathrm{g}}\boldsymbol{q}_{\mathrm{g}}T\right)\mathrm{d}V\\&\quad=\int_{\Omega}W_{\mathrm{T}}\cdot\left(-\Delta HR_{\mathrm{h}}-c_{\mathrm{T}}\frac{\mathrm{d}T}{\mathrm{d}t}\right)\mathrm{d}V\\&\qquad+\int_{\partial\Omega}W_{\mathrm{T}}\cdot\boldsymbol{n}\cdot\boldsymbol{q}_{\mathrm{T}}\mathrm{d}V,\end{aligned} \tag{64}$$

where S is the area of surface, and Ω stands for volume. $\boldsymbol{W}_{\mathrm{u}}$, $\boldsymbol{W}_{\mathrm{pw}}$, $\boldsymbol{W}_{\mathrm{pg}}$, and $\boldsymbol{W}_{\mathrm{T}}$ are the test functions for displacement $\boldsymbol{u}$, p_{w}, p_{g}, and T. Lagrange shape functions $\boldsymbol{N}_{\mathrm{u}}$, N_{pw}, N_{pg}, and N_{T} are used to build the FEM form.

$$\boldsymbol{K}_{\mathrm{uu}}:\boldsymbol{u}+\boldsymbol{K}_{\mathrm{upg}}p_{\mathrm{g}}+\boldsymbol{K}_{\mathrm{upw}}p_{\mathrm{w}}=\boldsymbol{F}_{\mathrm{u}}, \tag{65}$$

$$C_{\mathrm{pwu}}\frac{\mathrm{d}u}{\mathrm{d}t}+C_{\mathrm{pwpw}}\frac{\mathrm{d}p_{\mathrm{w}}}{\mathrm{d}t}+K_{\mathrm{pwpw}}p_{\mathrm{w}}+C_{\mathrm{pwpg}}\frac{\mathrm{d}p_{\mathrm{g}}}{\mathrm{d}t}+C_{\mathrm{pwT}}\frac{\mathrm{d}T}{\mathrm{d}t}=F_{\mathrm{pw}}, \tag{66}$$

$$C_{\mathrm{pgu}}\frac{\mathrm{d}u}{\mathrm{d}t}+C_{\mathrm{pgpw}}\frac{\mathrm{d}p_{\mathrm{w}}}{\mathrm{d}t}+K_{\mathrm{pgpg}}p_{\mathrm{g}}+C_{\mathrm{pgpg}}\frac{\mathrm{d}p_{\mathrm{g}}}{\mathrm{d}t}+C_{\mathrm{pgT}}\frac{\mathrm{d}T}{\mathrm{d}t}=F_{\mathrm{pg}}, \tag{67}$$

$$C_{\mathrm{TT}}\frac{\mathrm{d}T}{\mathrm{d}t}+K_{\mathrm{TT}}T+K_{\mathrm{TTpw}}T+K_{\mathrm{TTpg}}T=F_{\mathrm{T}}, \tag{68}$$

where

$$\boldsymbol{K}_{\mathrm{uu}}=\int_{\Omega}\nabla\cdot\boldsymbol{W}_{\mathrm{u}}\cdot\left(\boldsymbol{D}-\boldsymbol{D}:\frac{\partial\boldsymbol{\varepsilon}^{\mathrm{p}}}{\partial\boldsymbol{\varepsilon}}\right):\boldsymbol{L}:\boldsymbol{N}_{\mathrm{u}}\mathrm{d}V,$$

$$\boldsymbol{K}_{\mathrm{upg}}=\int_{\Omega}\nabla\cdot\boldsymbol{W}_{\mathrm{u}}\cdot\left(-\frac{s_{\mathrm{g}}N_{\mathrm{pg}}}{s_{\mathrm{w}}+s_{\mathrm{g}}}\boldsymbol{\delta}\right)\mathrm{d}V,$$

$$\boldsymbol{K}_{\mathrm{upw}}=\int_{\Omega}\nabla\cdot\boldsymbol{W}_{\mathrm{u}}\cdot\left(-\frac{s_{\mathrm{w}}N_{\mathrm{pw}}}{s_{\mathrm{w}}+s_{\mathrm{g}}}\boldsymbol{\delta}\right)\mathrm{d}V,$$

$$\boldsymbol{F}_{\mathrm{u}}=\int_{\partial\Omega}\boldsymbol{W}_{\mathrm{u}}\cdot\boldsymbol{t}\cdot\boldsymbol{N}_{\mathrm{t}}\mathrm{d}S+\int_{\Omega}\boldsymbol{W}_{\mathrm{u}}\cdot\boldsymbol{f}\cdot\boldsymbol{N}_{\mathrm{f}}\mathrm{d}V,$$

$$C_{\mathrm{pwu}}=\int_{\Omega}W_{\mathrm{pw}}\left(s_{\mathrm{w}}-s_{\mathrm{h}}\frac{\partial s_{\mathrm{w}}}{\partial s_{\mathrm{h}}}\right)\boldsymbol{\delta}:\boldsymbol{L}:\boldsymbol{N}_{\mathrm{u}}\mathrm{d}V,$$

$$C_{\mathrm{pwpw}}=\int_{\Omega}W_{\mathrm{pw}}\left(\frac{n_{\mathrm{w}}}{B_{\mathrm{w}}}-n\frac{\partial s_{\mathrm{w}}}{\partial s_{\mathrm{e}}}\frac{\mathrm{d}s_{\mathrm{e}}}{\mathrm{d}p_{\mathrm{c}}}\right)N_{\mathrm{pw}}\mathrm{d}V,$$

$$K_{\mathrm{pwpw}}=\int_{\Omega}\nabla W_{\mathrm{pw}}\frac{K_{\mathrm{h}}k_{\mathrm{w}}}{\mu_{\mathrm{w}}}(\nabla N_{\mathrm{pw}})\mathrm{d}V,$$

$$C_{\mathrm{pwpg}}=\int_{\Omega}W_{\mathrm{pw}}\left(n\frac{\partial s_{\mathrm{w}}}{\partial s_{\mathrm{e}}}\frac{\mathrm{d}s_{\mathrm{e}}}{\mathrm{d}p_{\mathrm{c}}}N_{\mathrm{pg}}\right)\mathrm{d}V,$$

$$C_{\mathrm{pwT}}=\int_{\Omega}W_{\mathrm{pw}}\left(-n\left(n_{\mathrm{w}}\beta_{\mathrm{w}}-n_{\mathrm{h}}\beta_{\mathrm{h}}\frac{\partial s_{\mathrm{w}}}{\partial s_{\mathrm{h}}}\right)N_{\mathrm{T}}\right)\mathrm{d}V,$$

$$F_{\mathrm{pw}}=\int_{\Omega}\nabla W_{\mathrm{pw}}\cdot\frac{K_{\mathrm{h}}k_{\mathrm{w}}\rho_{\mathrm{w}}}{\mu_{\mathrm{w}}}\boldsymbol{g}\mathrm{d}V+\int_{\Omega}W_{\mathrm{pw}}\left(6\frac{1}{\rho_{\mathrm{w}}}M_{\mathrm{w}}+\frac{1}{\rho_{\mathrm{h}}}\frac{\partial s_{\mathrm{w}}}{\partial s_{\mathrm{h}}}M_{\mathrm{h}}\right)R_{\mathrm{h}}\mathrm{d}V+\sum_{i}\int_{\partial\Omega}W_{\mathrm{pw}}\boldsymbol{n}\cdot N_{\mathrm{pw}}\cdot\boldsymbol{q}_{\mathrm{w}}\mathrm{d}S,$$

$$C_{\mathrm{pgu}}=\int_{\Omega}W_{\mathrm{pg}}\left(s_{\mathrm{g}}-\frac{s_{\mathrm{h}}\partial s_{\mathrm{g}}}{\partial s_{\mathrm{h}}}\right)\boldsymbol{\delta}:\boldsymbol{L}:\boldsymbol{N}_{\mathrm{u}}\mathrm{d}V,$$

$$C_{\mathrm{pgpw}}=-\int_{\Omega}W_{\mathrm{pg}}n\frac{\partial s_{\mathrm{g}}}{\partial s_{\mathrm{e}}}\frac{\mathrm{d}s_{\mathrm{e}}}{\mathrm{d}p_{\mathrm{c}}}N_{\mathrm{pw}}\mathrm{d}V,$$

$$C_{\mathrm{pgpg}}=-\int_{\Omega}W_{\mathrm{pg}}\left(\frac{n_{\mathrm{g}}}{B_{\mathrm{g}}}+\frac{n\partial s_{\mathrm{g}}}{\partial s_{\mathrm{e}}}\frac{\mathrm{d}s_{\mathrm{e}}}{\mathrm{d}p_{\mathrm{c}}}\right)N_{\mathrm{pg}}\mathrm{d}V,$$

$$K_{\mathrm{pgpg}}=\int_{\Omega}\nabla W_{\mathrm{pg}}\left(\frac{K_{\mathrm{h}}k_{\mathrm{g}}}{\mu_{\mathrm{g}}}\right)\nabla N_{\mathrm{pg}}\mathrm{d}V,$$

$$C_{\mathrm{pgT}}=\int_{\Omega}W_{\mathrm{pg}}n\left(n_{\mathrm{h}}\beta_{\mathrm{h}}\frac{\partial s_{\mathrm{g}}}{\partial s_{\mathrm{h}}}-n_{\mathrm{g}}\beta_{\mathrm{g}}\right)N_{\mathrm{T}}\mathrm{d}V,$$

$$F_{\mathrm{pg}}=\int_{\Omega}W_{\mathrm{pg}}\left(\frac{1}{\rho_{\mathrm{g}}}M_{\mathrm{g}}+\frac{1}{\rho_{\mathrm{h}}}\frac{\partial s_{\mathrm{g}}}{\partial s_{\mathrm{h}}}M_{\mathrm{h}}\right)R_{\mathrm{h}}\mathrm{d}V+\int_{\Omega}\nabla W_{\mathrm{pg}}\cdot\frac{K_{\mathrm{h}}k_{\mathrm{g}}\rho_{\mathrm{g}}}{\mu_{\mathrm{g}}}\boldsymbol{g}\mathrm{d}V+\int_{\partial\Omega}W_{\mathrm{pg}}\boldsymbol{n}\cdot N_{\mathrm{pg}}\boldsymbol{q}_{\mathrm{g}}\mathrm{d}S,$$

$$C_{\mathrm{TT}}=\int_{\Omega}W_{\mathrm{T}}c_{\mathrm{T}}N_{\mathrm{T}}\mathrm{d}V,$$

$$K_{\mathrm{TT}}=\int_{\Omega}\nabla W_{\mathrm{T}}\left[K_{\mathrm{T}}\nabla N_{\mathrm{T}}+\left(c_{\mathrm{w}}\rho_{\mathrm{w}}\frac{K_{\mathrm{h}}k_{\mathrm{w}}\rho_{\mathrm{w}}\boldsymbol{g}}{\mu_{\mathrm{w}}}+c_{\mathrm{g}}\rho_{\mathrm{g}}\frac{K_{\mathrm{h}}k_{\mathrm{g}}\rho_{\mathrm{g}}\boldsymbol{g}}{\mu_{\mathrm{g}}}\right)N_{\mathrm{T}}\right]\mathrm{d}V,$$

$$K_{\mathrm{TTpw}}=\int_{\Omega}\nabla W_{\mathrm{T}}\left(c_{\mathrm{w}}\rho_{\mathrm{w}}\frac{K_{\mathrm{h}}k_{\mathrm{w}}}{\mu_{\mathrm{w}}}\nabla N_{\mathrm{pw}}p_{\mathrm{w}}N_{\mathrm{T}}\right)\mathrm{d}V,$$

$$K_{\mathrm{TTpg}}=\int_{\Omega}\nabla W_{\mathrm{T}}\left(c_{\mathrm{g}}\rho_{\mathrm{g}}\frac{K_{\mathrm{h}}k_{\mathrm{g}}}{\mu_{\mathrm{g}}}\nabla N_{\mathrm{pg}}p_{\mathrm{g}}N_{\mathrm{T}}\right)\mathrm{d}V,$$

$$F_{\mathrm{T}}=\int_{\Omega}W_{\mathrm{T}}\left(-\Delta HR_{\mathrm{h}}\right)\mathrm{d}V+\int_{\partial\Omega}W_{\mathrm{T}}\boldsymbol{n}\cdot N_{\mathrm{pT}}\boldsymbol{q}_{\mathrm{T}}\mathrm{d}V,$$

where $\boldsymbol{t}$ is the traction force, and $\boldsymbol{N}_{\mathrm{t}}$ and $\boldsymbol{N}_{\mathrm{f}}$ are the shape functions for the traction force and body force, respectively.

The IDA solver embedded in COMSOL is used to solve the nonlinear ordinary differential equations, in which back differential form is implemented. The details are given in COMSOL Mutiphysics® documentation (COMSOL, 2017). The mechanical behavior is modeled using the structural mechanical module in COMSOL. Fig. 1 shows the configuration of the external material interface. The updated variables or parameters such as hydrate saturation are fed into the external material interface using material parameters in COMSOL.

4 Verification of the thermo-hydro-chemical part of the COMSOL code

The hydrate dissociation experiment data produced by Masuda et al. (1999) were used to verify the performance of the coupled THMC code. Table 1 shows the conditions of this experiment. We assumed that the initial distributions of phase saturation, pressure, and temperature were uniform in the core homogeneous sample. Fig. 2 (p.610) shows the mesh and boundary conditions of the model in which depressurization is applied at the left boundary. There is a heat supply from the top outside boundary. Because Masuda et al. (1999) conducted the experiment in a hot water bath, the formulation of heat flux was applied $q_{\mathrm{in}}=h(T_{\mathrm{c}}-T)$, where T_{c} is the circumstance temperature and h is the heat transfer coefficient of the reactor wall. The changes of temperature at sections A, B, and C in the model were investigated.

Fig. 3 (p.610) shows the amount of gas production calculated using this model, and the experimental data given by Masuda et al. (1999). Because of the lack of material information about the reactor wall, the heat transfer coefficient of the reactor wall was varied to match the amount of gas production.

Fig. 4 (p.610) shows the changes of temperature during gas production at the three monitoring locations. The comparison shows that not only the amount of gas production, but also the variation of temperature can be well simulated using this model. The gas production becomes slower with decreasing hydrate saturation because the dissociation rate is affected by hydrate saturation, as shown in Eq. (4).

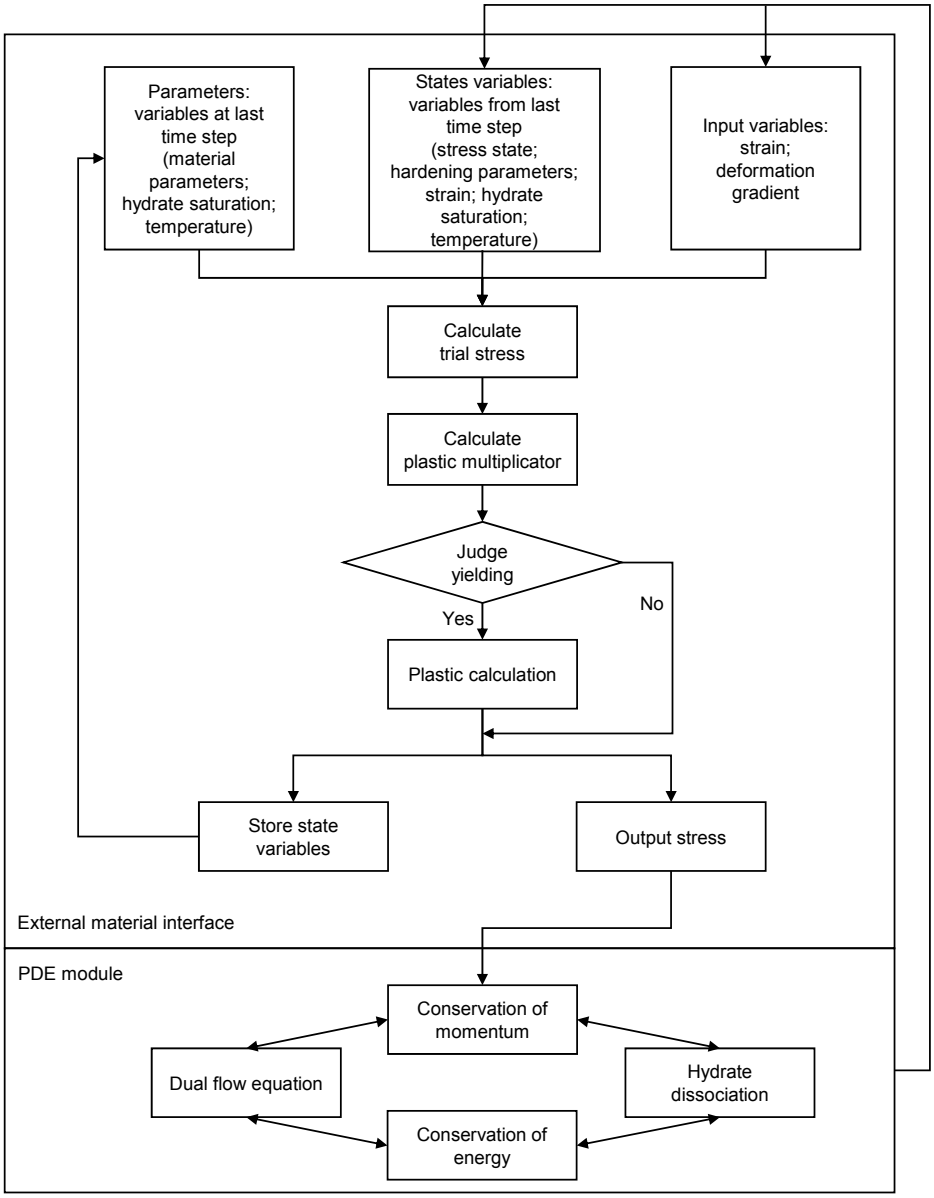

Fig. 1 Configuration of the external material interface

Table 1 Experimental conditions in the hydrate dissociation experiment of Masuda et al. (1999)

Initial and boundary conditions	Value
Porosity, n_0	0.182
Initial water saturation, s_{w0}	0.206
Initial pressure, p_0 (MPa)	3.75
Initial temperature, T_0 (K)	275.45
Circumstance temperature, T_c (K)	275.45
Initial gas saturation, s_{g0}	0.351
Outlet pressure, p_{out} (MPa)	2.84
Heat transfer coefficient of reactor wall, h (W/(m^2·K))	25

The temperature initially decreases because hydrate dissociation is an endothermic process. However, due to heat supply from the outside, the temperature then increases.

An international collaborative effort compared seven different hydrate reservoir simulators, HydrateResSim, MH-21 HYDRES, STARS-OIL, STARSSOLID, STOMP-HYD, TOUGH-FX/HYDRATE, and a code from the University of Houston, USA (Wilder et al., 2008). The simulators were coupled thermo-hydro-chemical formulations that did not

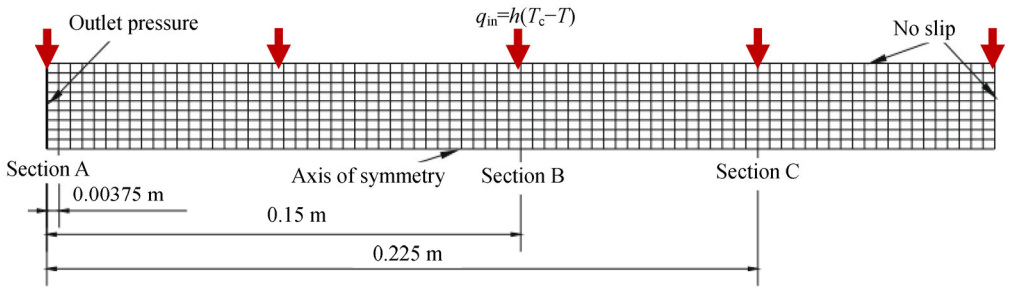

Fig. 2 Sketch of the numerical model for the specimen

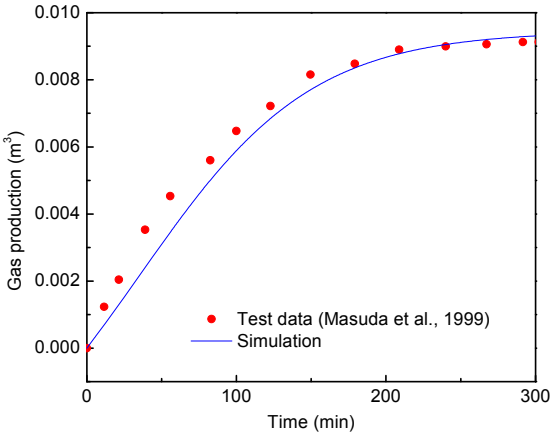

Fig. 3 Comparison between the amount of gas production from simulation and experiment

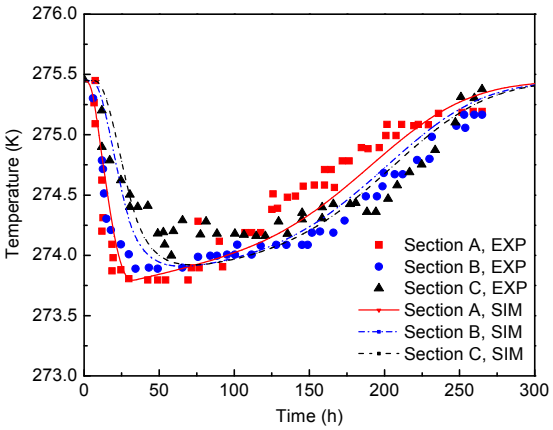

Fig. 4 Comparison between temperatures in simulations (SIM) and experiment (EXP)

consider mechanical behavior. Fig. 5 shows a comparison of the COMSOL fully coupled THMC model to the other seven simulators for the problem of thermal injection (Problem 3, Case 1 of Wilder et al. (2008)). Fig. 6 (p.612) gives the comparison for the case of depressurization (Problem 3, Case 2 of Wilder et al. (2008)). The boundary conditions and parameters are identical to those of Wilder et al. (2008). The comparisons include hydrate saturation, gas saturation, and temperature after 1 h, 1 d, and 2 d, to validate the coupling method regarding hydrate dissociation, gas and water flow in porous media, and heat flow during dissociation. Results show good agreement between the COMSOL fully coupled thermo-hydro-chemical formulation and the other seven simulations in terms of hydrate saturation and temperature. However, for gas saturation, different results were obtained using different simulators, and the COMSOL model produced a relatively large value. This difference arose mainly because different effective saturation definitions, capillary pressures, and relative permeability models are applied in the different models. Many of them use Stone and Aziz or Corey's relative permeability model rather than the van Genuchten model used in our model. The use of a soil-water characteristic curve with a lower curve slope tends to result in a lower gas saturation because it becomes difficult to drain the pore water from the soil and the soil is more saturated. Because of the lack of test data about relative permeability of hydrate bearing sediments, the uncommon material parameters used in different codes differ. The uncommon material parameters used in the study by Wilder et al. (2008) were not identified. Here, the results simply demonstrate that the same changing trend for each variable can be obtained using our model. For a more precise description, more published test data are needed.

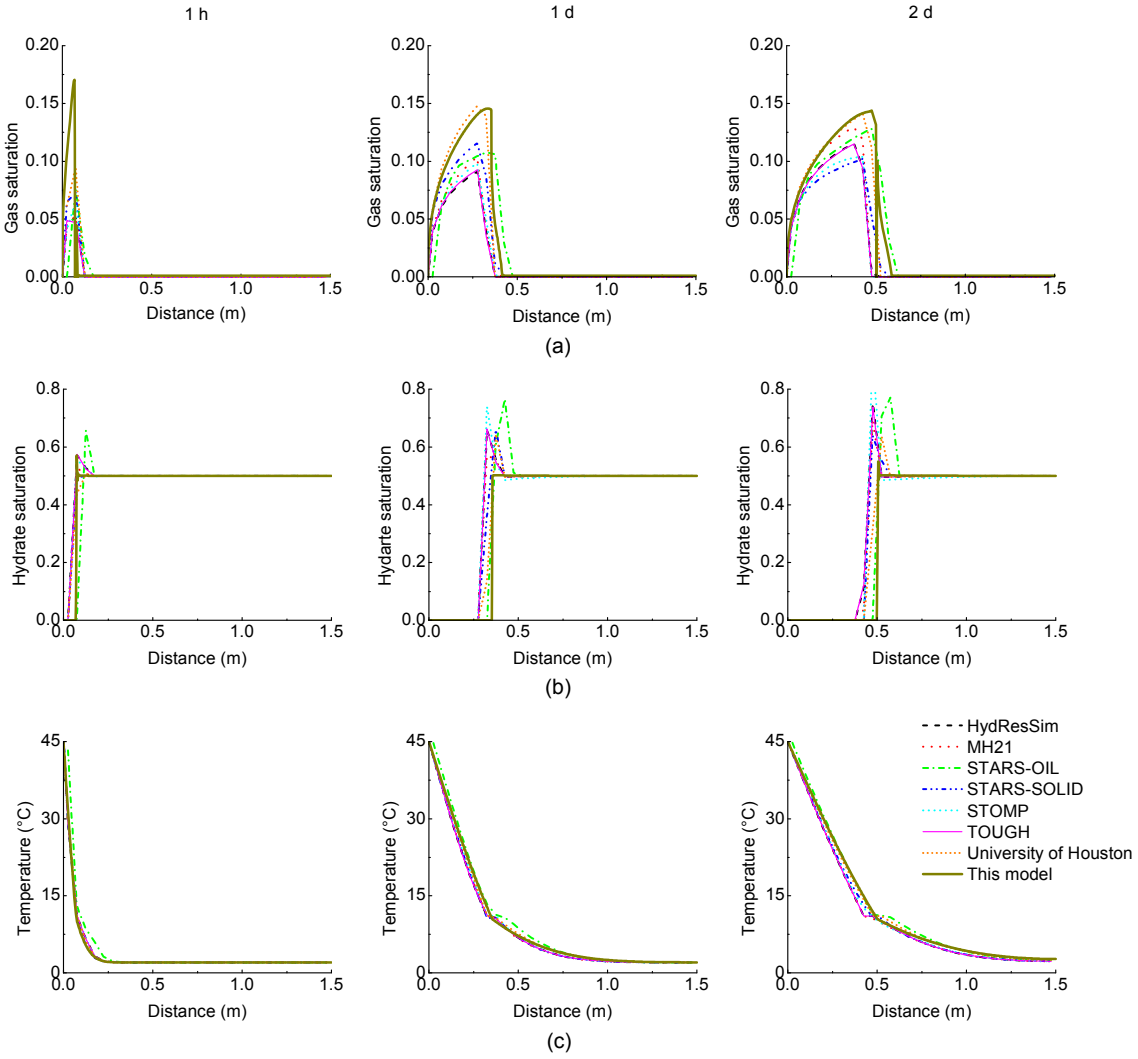

Fig. 5 Comparison of simulations with different codes in the heat injection case after 1 h, 1 d, and 2 d
(a) Gas saturation; (b) Hydrate saturation; (c) Temperature

5 Performance of the mechanical model of COMSOL

Masui et al. (2006, 2007) conducted a series of drained triaxial compression tests using synthetic hydrate-bearing sediments from Toyoura sand and natural core samples from the Nankai Trough to determine the stress-strain relationship of natural MHBS. Hyodo et al. (2013a, 2013b) conducted a series of tests to study the mechanical properties of MHBS. The host sand was Toyoura sand. For the purpose of verification, in this study we used these three datasets to examine the performance of the proposed constitutive model.

The values of the best-fitted model parameters are listed in Table 2 for the synthetic hydrate-bearing sediment specimens. The simulated results using the new TMH model and the methane hydrate critical state (MHCS) model by Uchida et al. (2012) are shown in Fig. 7. Fig. 7a presents the stress-strain relationship of pore filling, cementing, and no hydrate, and Fig. 7b shows the volume change behavior during shearing. By adjusting the parameters α and γ in the new TMH model, the predicted stress-strain curve and the dilatancy curve closely match the test data. These two parameters governing the shape of yield loci and the ratio of the dilatancy part to the contraction part on the yield loci can be obtained by

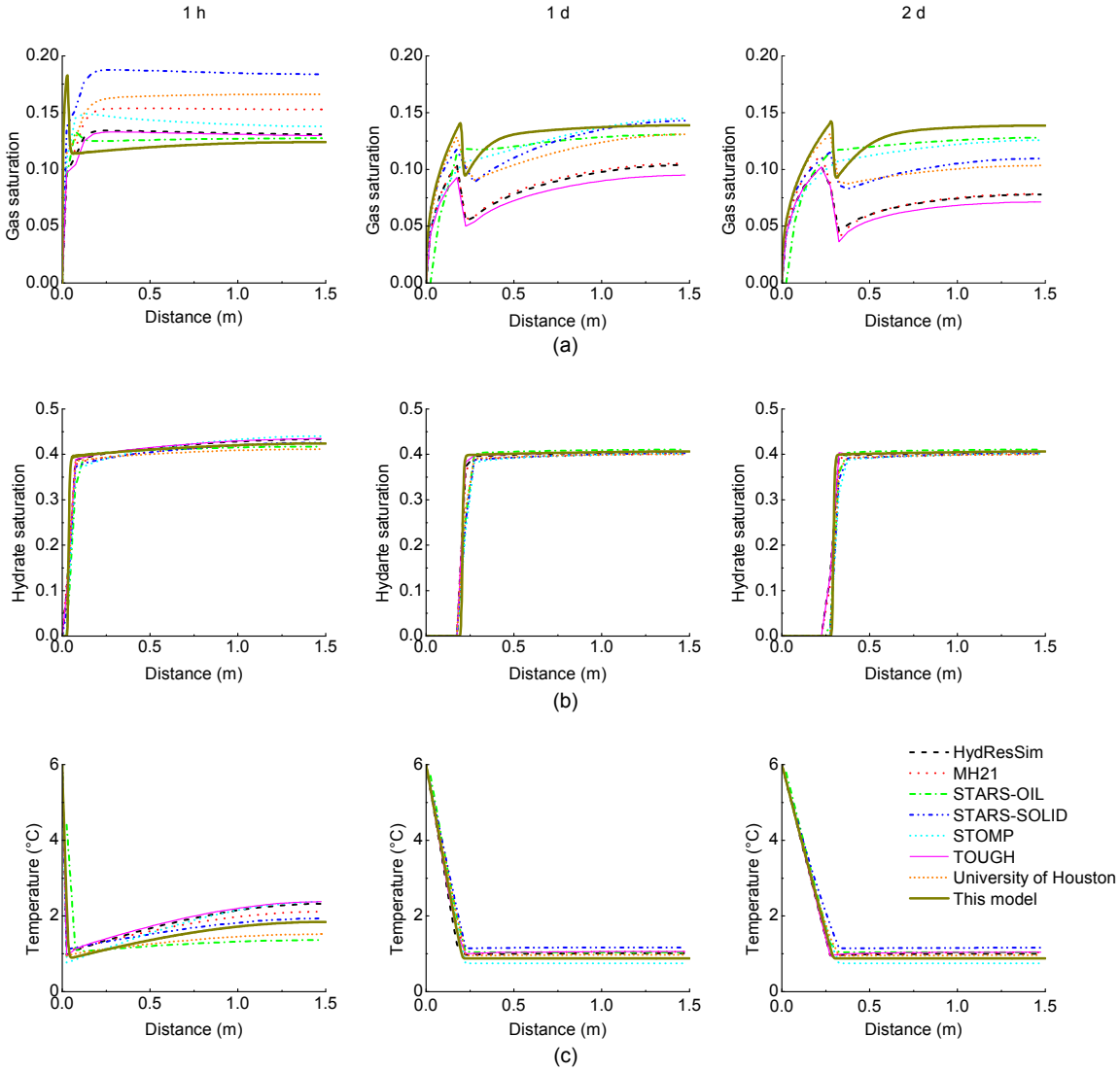

Fig. 6 Comparison of simulations with different codes in the depressurization case after 1 h, 1 d, and 2 d
(a) Gas saturation; (b) Hydrate saturation; (c) Temperature

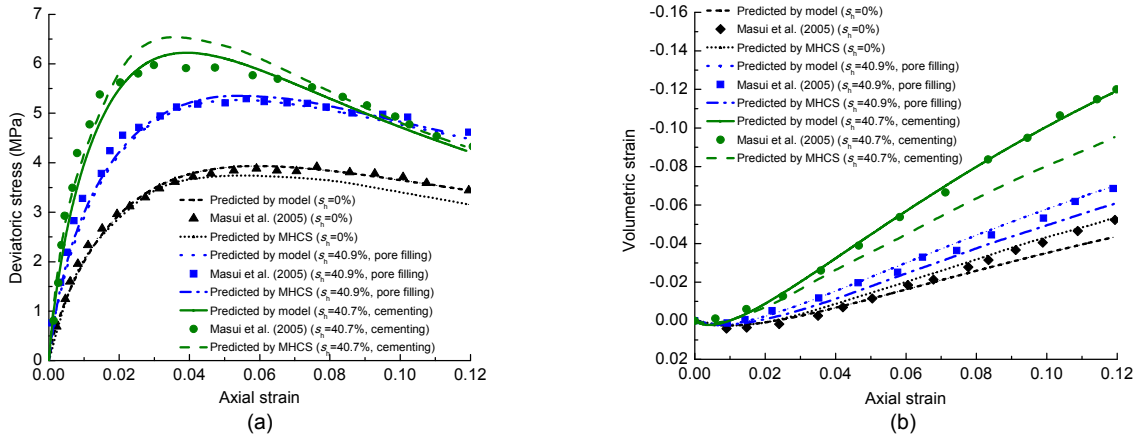

Fig. 7 Drained triaxial stress-strain relationship (a) and dilatancy curve (b) of Toyoura sand

Table 2 Parameters for synthetic hydrate sediment

Parameter	Value
Poisson's ratio, μ	0.2
Preconsolidation pressure, p_{cs0} (MPa)	12
M	1.07
m	1 (pore-filling); 3 (cementing)
λ	0.16
κ	0.004
γ	0.9 (s_h=0); 1.0 (pore-filling); 1.13 (cementing)
α	1.1 (s_h=0); 1 (pore filling); 0.7 (cementing)
Initial structure factor, χ_0	1
a	14 (pore filling); 42 (cementing)
b	1.6
c	0.8 (pore filling); 0.1 (cementing)
d	1
u	18
m_2 (MPa)	250 (pore filling); 850 (cementing)
v	1.59
s_h	0.409 (pore filling); 0.407 (cementing)

undrained (zero volumetric strain) tests or by matching the drained triaxial stress-strain curve and the dilatancy curve.

Fig. 8 shows the simulated results for hydrate saturation, pressure, temperature, volumetric strain, mean effective stress, and deviator stress during depressurization calculated using the new TMH model and the MHCS model, where r is the radius, and r_{well} is the radius of the wellbore. The presence of hydrate enhances the strength, stiffness, and dilatancy of sediments by making the sediments denser and bonded. The sediments of different hydrate types present different stress-strain and dilatancy relationships. Cementing type sediments have higher strength and are more dilatant. The variation of hydrate saturation, pressure, and temperature is governed by the flow equations, and the results calculated by the two models are similar. For volumetric strain, mean effective stress, and deviator stress, some differences are observed. The increase in mean effective stress due to depressurization calculated by the MHCS model is faster than that of the TMH model, because the yield surfaces and flow rule of the TMH model differ from those of the MHCS model. The value of γ we used expanded the wet side of the yield loci and increased the yield deviator stress. It also increased the dilatancy ratio, making volume contraction difficult. Further details are given by Sun et al. (2015). Parameter γ governs the dilatant behavior and yield loci by changing the ratio of the dry side to the wet side of the yield surface (Sun et al., 2015). When the mean effective stress is the same, the MHCS model computes a larger deviator stress than the TMH model (Fig. 7). This is because yielding occurs earlier in the TMH model by adjusting the parameter γ. Because the computed mean effective stress is larger in the MHCS model than in the TMH model, larger volumetric strain values are obtained with the MHCS model than with the TMH model.

6 Fully coupled versus semi-coupled THMC models

Many semi-coupled THMC models have been proposed, most of which are FVM models (Moridis et al., 2004; Klar et al., 2010; Kakumoto et al., 2011a). In these models, the force balance equations and the flow equations are calculated separately. Firstly, the pressure field is obtained from the calculation of the flow equation. Then, through the effective stress principle, continuity equations, and constitutive model, displacement can be solved. Although volumetric change due to the change in the effective stress state affects liquid flow behavior, many FVM models do not consider the impact of volumetric change on flow behavior. In this section, the differences in the simulation results between the fully coupled THMC model and the semi-coupled model are discussed.

The parameters of the model are shown in Table 3 (p.615), and the mesh is presented in Fig. 9. The radius of the well is 0.15 m. Water pressure near the well decreases from 13 MPa to 7 MPa in 2 d. We assumed that the temperature at the wellbore side was

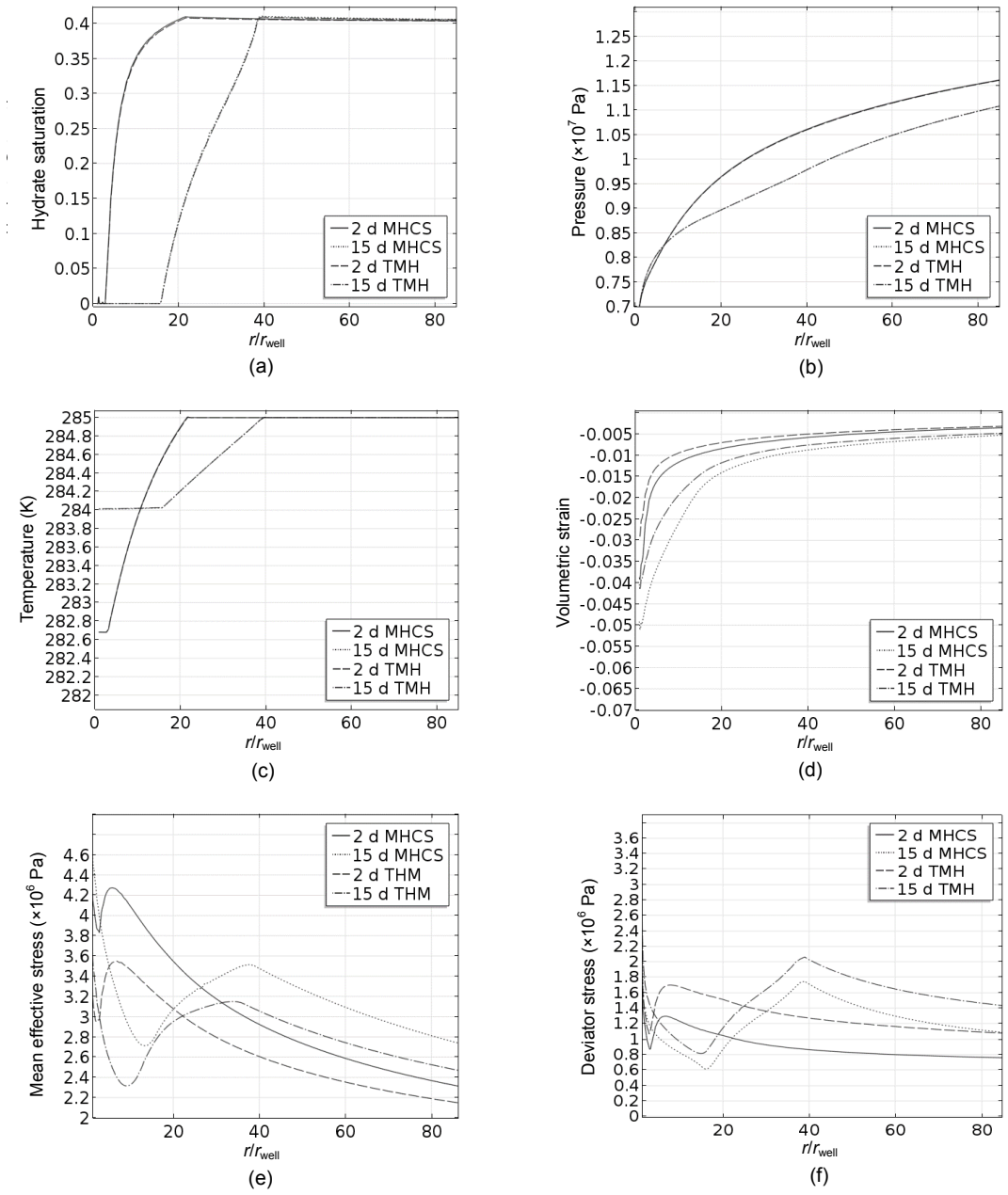

Fig. 8 Comparisons between the TMH and MHCS models: (a) hydrate saturation; (b) pressure; (c) temperature; (d) volumetric strain; (e) mean effective stress; (f) deviator stress

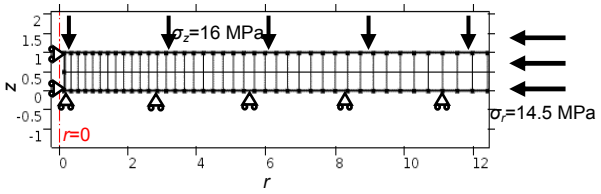

Fig. 9 Mesh of the model close to the wellbore

σ_r is the radial normal stress, and σ_z is normal stress in the z direction

equal to that of the soil close to the wellbore. The temperature at the far-end boundary was set to be equal to the initial temperature because we assumed that there was enough heat supply in the far field. The differences between the fully coupled and the semi-coupled models are shown through the impact of variation in porosity and volumetric strain on the flow and heat equations. In the fully coupled THMC model, porosity and volumetric strain are updated

every time step and influence the flow and heat properties. However, in the semi-coupled THMC model, porosity and volumetric strain remain constant in the flow and heat equations, without any impact on the flow and heat properties.

Table 3 Parameters of the model

Parameter	Description
n_0	0.35
B_w (GPa)	2
B_g	p_g
p_0 (kPa)	10
n_1, n_2, n_3	0.8, 0.5, 0.5
K (m^2)	10^{-13}
N	8
K_{d0} (mol/(m^2·Pa·s))	1.24×10^5
ΔE_d (J/mol)	−78 300
K_{Ts} (W/(m·K))	3.92
ρ_s (kg/m^3)	2800
ρ_w (kg/m^3)	1000
μ	0.3
p_{cs0} (MPa)	4.5
M	1.35
m	4
m_2 (MPa)	200
γ	0.85
λ	0.1
κ	0.006
K_{Tw} (W/(m·K))	0.556
K_{Tg} (W/(m·K))	0.0335
K_{Th} (W/(m·K))	0.394
β_w (K^{-1})	$13.41T-3717$
β_g (K^{-1})	$1/T$
β_h (K^{-1})	4.6×10^{-4}
c_s (J/(g·K))	0.8
c_w (J/(g·K))	$4.02+0.000\,577T$
c_g (J/(g·K))	$1.24+0.003\,13T$
c_h (J/(g·K))	2.01
N_h	6
P_{eq}	$e^{39.08-8520/T}$
ρ_h (kg/m^3)	800
χ_0	1
a	20
b	1
c	0.1
d	1
u	30
α	1

Fig. 10 shows the change in hydrate saturation during depressurization. At the beginning of depressurization, hydrate saturation increases in the fully coupled THMC model, but does not change in the semi-coupled THMC model. This is because, in the fully coupled model, the volumetric strain change due to the compression by depressurization is updated at every time step and hydrate saturation is re-calculated using the updated volumetric strain. In reality, the volume contraction of host sediments increases the hydrate volume fraction and decreases the space of the void in which the fluid can flow through the formation.

As hydrate dissociates, the hydrate saturation in the semi-coupled THMC model drops faster than that in the fully coupled THMC model, because the fully

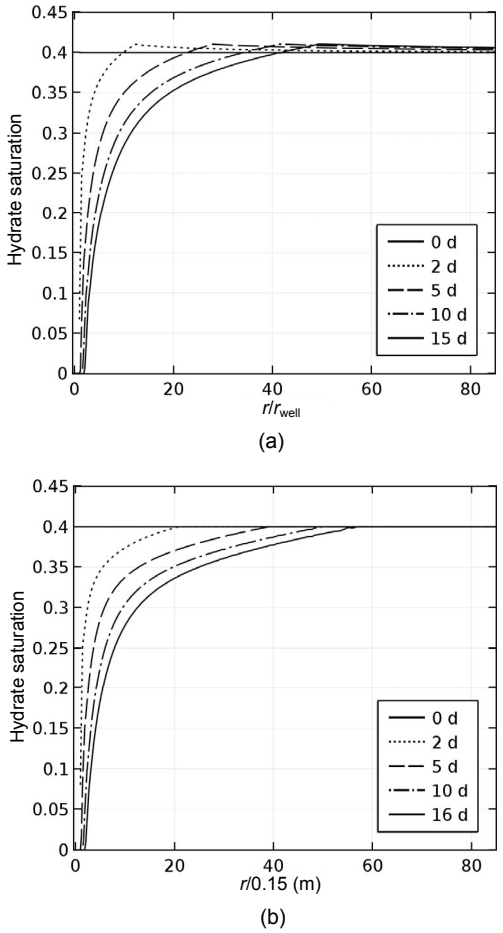

Fig. 10 A comparison of hydrate saturation calculated using fully coupled and semi-coupled THMC models
(a) Fully coupled THMC model; (b) Semi-coupled THMC model

coupled model gives a slower depressurization rate. The difference is clearly shown in Fig. 11, which shows the change in pore pressure during depressurization. As the formation compaction reduces the space for water and gas flow, the pore pressure decreases more slowly in the fully coupled THMC model than in the semi-coupled THMC model.

Fig. 12 shows that hydrate dissociates faster in the semi-coupled THMC model than in the fully coupled THMC model. Consequently, temperature drops more quickly in the semi-coupled THMC model. For the mechanical part, pore pressure has a great impact on the force balance according to the effective stress principle. Fig. 13 shows that the mean effective stress is greater in the semi-coupled THMC model than that in the fully coupled THMC model for a given time, as pore pressure decreases faster in the semi-coupled THMC model. Fig. 14 shows that changes in deviator stress near the well boundary are greater in the semi-coupled model because the mean effective stress is higher than that in the fully coupled THMC model. Larger volume contraction can be obtained using the semi-coupled THMC model. Because of the circumferential restriction, the circumferential stress decreases more with the larger volume contraction in the semi-coupled THMC model, leading to a larger difference between vertical stress and circumferential stress. Fig. 15 shows that the volumetric strains in the semi-coupled THMC model are larger than those in the fully coupled THMC model because the mean effective stress is larger in the semi-coupled THMC model.

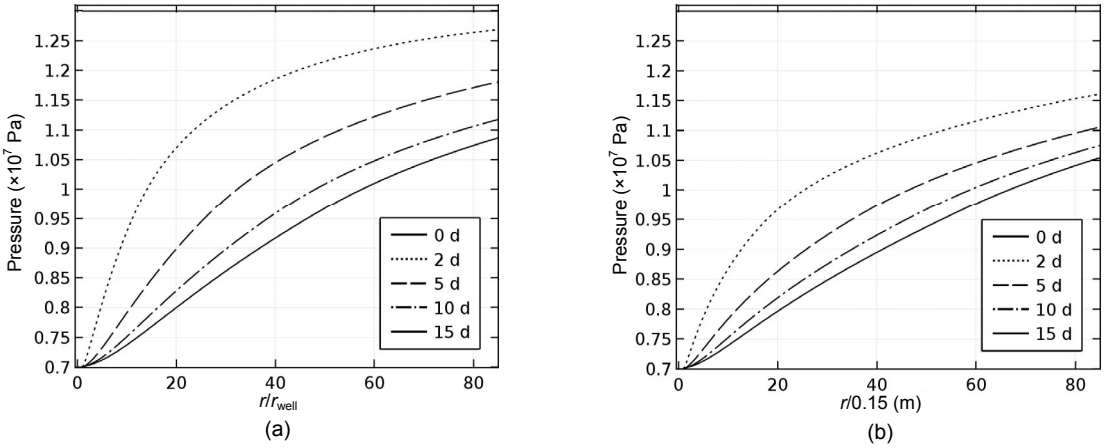

Fig. 11 A comparison of pressure calculated using fully coupled and semi-coupled THMC models
(a) Fully coupled THMC model; (b) Semi-coupled THMC model

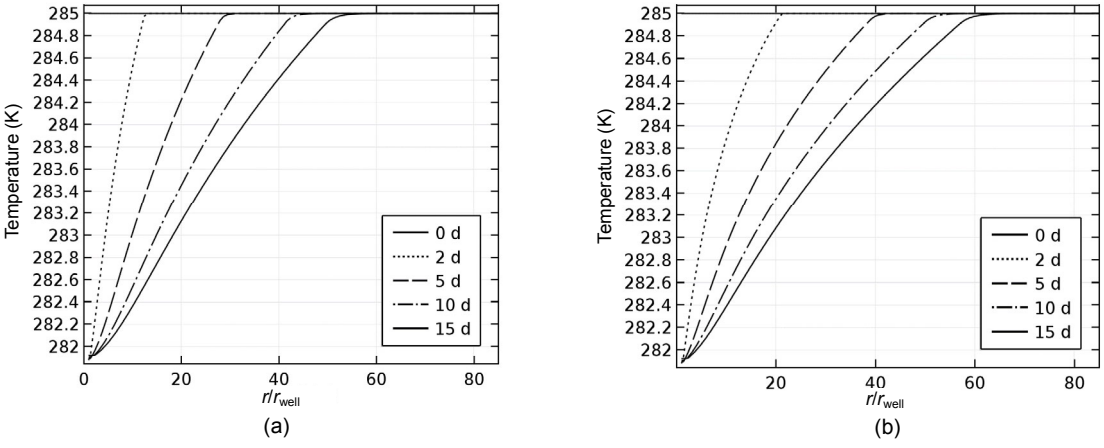

Fig. 12 A comparison of temperature calculated using fully coupled and semi-coupled THMC models
(a) Fully coupled THMC model; (b) Semi-coupled THMC model

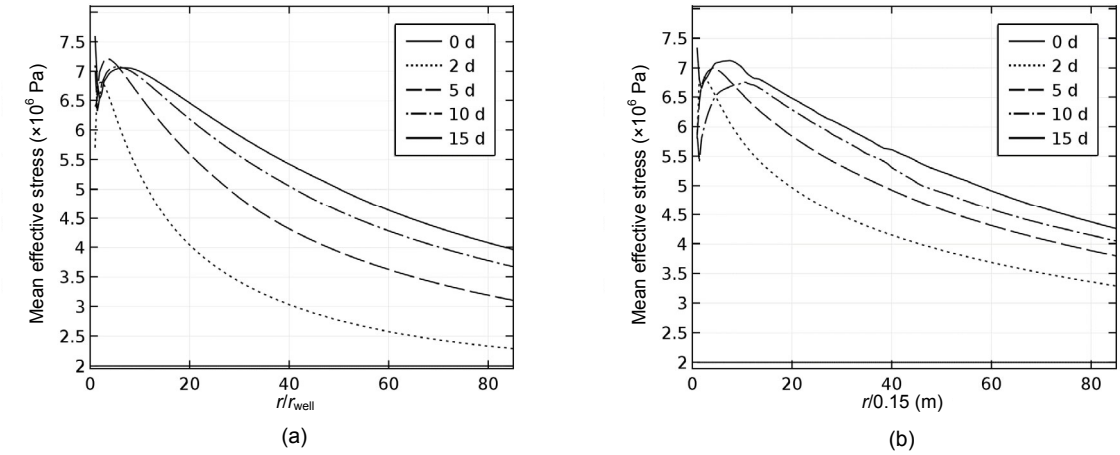

Fig. 13 A comparison of mean effective stress calculated using fully coupled and semi-coupled THMC models
(a) Fully coupled THMC model; (b) Semi-coupled THMC model

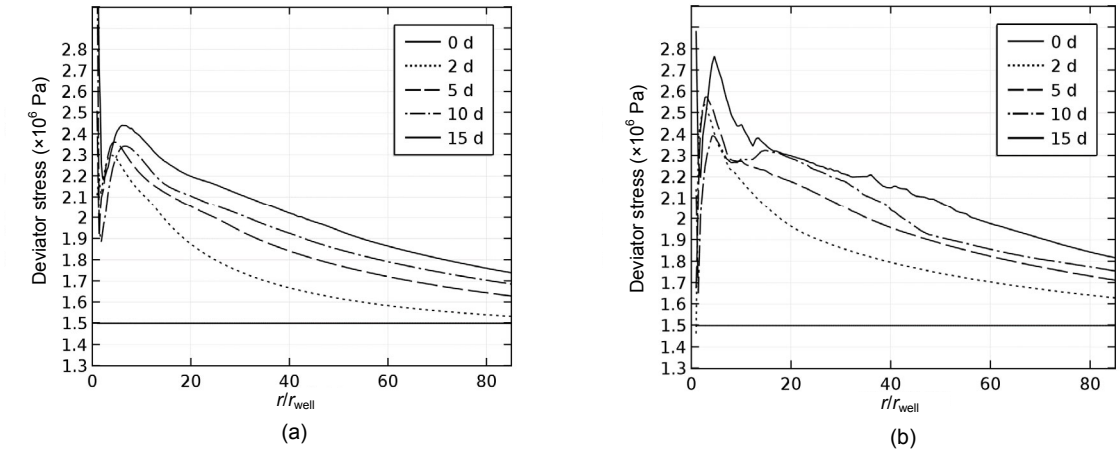

Fig. 14 A comparison of deviator stress calculated using fully coupled and semi-coupled THMC models
(a) Fully coupled THMC model; (b) Semi-coupled THMC model

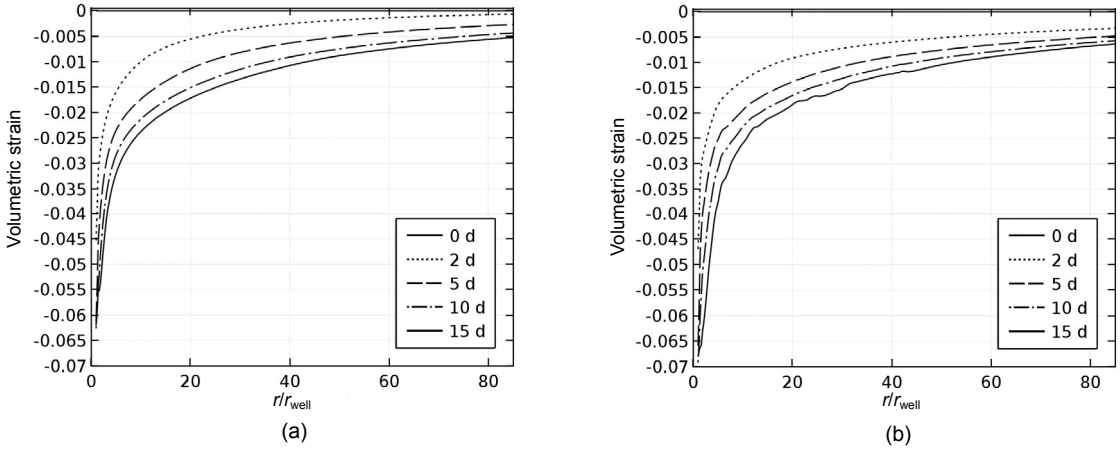

Fig. 15 A comparison of volumetric strain calculated using fully coupled and semi-coupled THMC models
(a) Fully coupled THMC model; (b) Semi-coupled THMC model

7 Simulation of hydrate production by depressurization

In this section, a depressurization process for extracting methane gas from a sediment layer with a specific heterogeneous hydrate distribution is simulated. The model is shown in Fig. 16. The hydrate distribution is shown in Fig. 17a. The interbedded layer without hydrate is clay and the intrinsic permeability is different in the different layers (Fig. 17b).

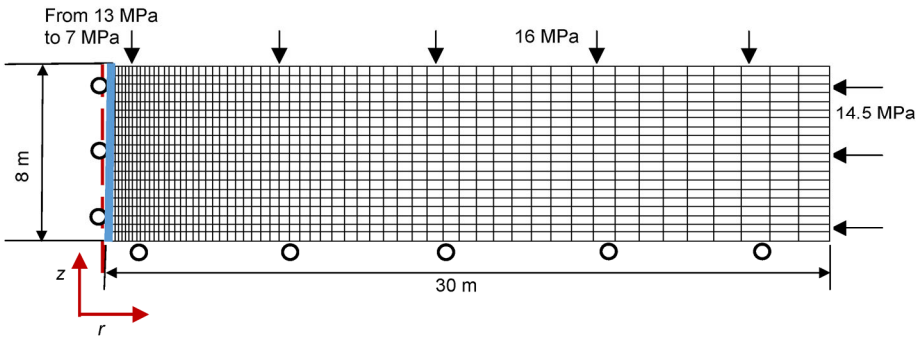

Fig. 16 An assumed vertical well model

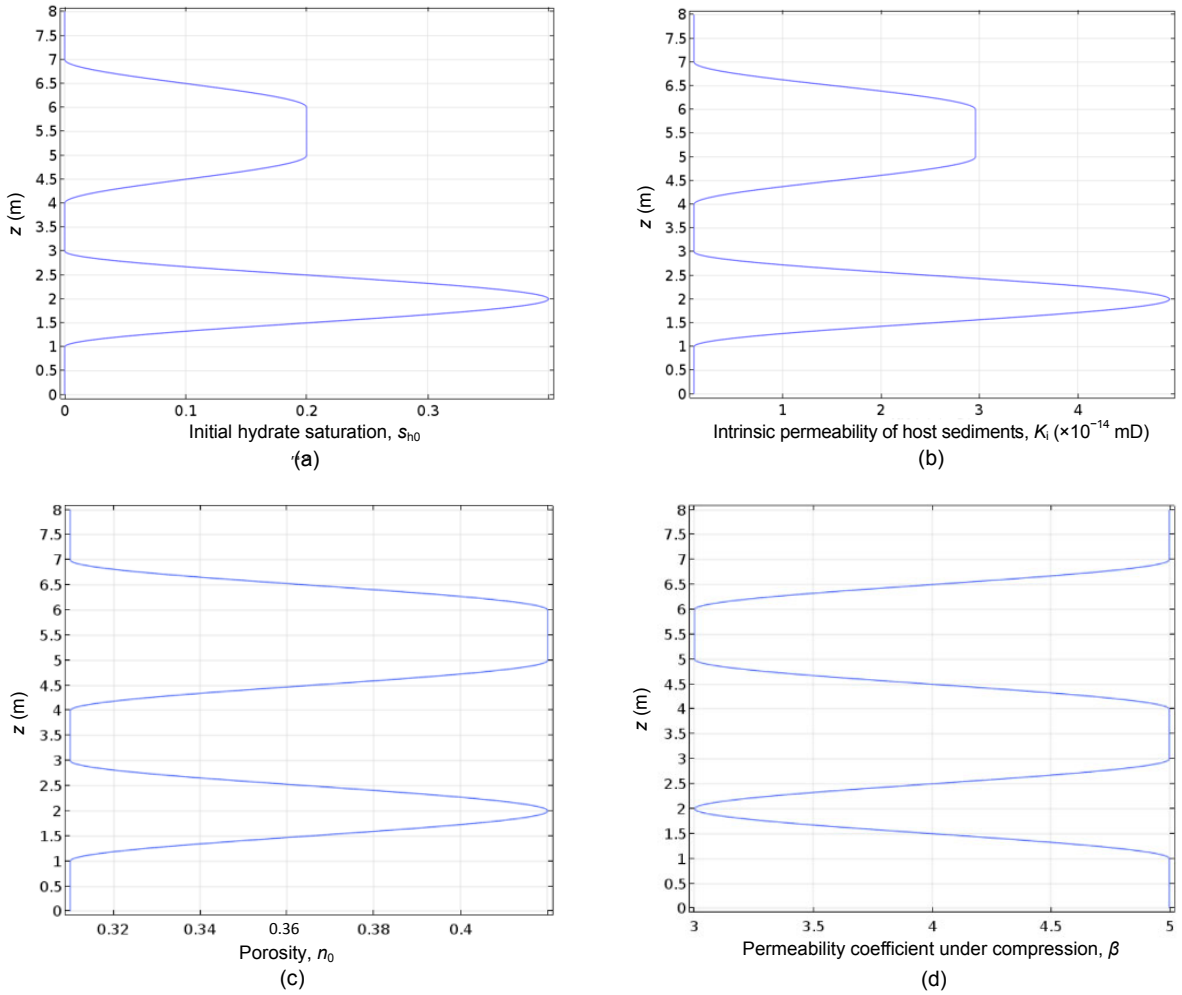

Fig. 17 Initial hydrate saturation and intrinsic permeability distribution along the vertical
(a) Hydrate saturation; (b) Intrinsic permeability; (c) Porosity; (d) Empirical formula parameter

The porosity distribution is shown in Fig. 17c. A power law-type empirical formula was adopted for the relationship between the void ratio and permeability, as presented in Eq. (25). The distribution of the parameter related to permeability in Eq. (25) is shown in Fig. 17d and the value was chosen according to Sakamoto et al. (2010). The water pressure at the left boundary of the model decreases from 13 MPa to 7 MPa in 2 h to model the depressurization inside the well. When the wellbore pressure is 8.7 MPa, hydrate in the formation starts to dissociate. We assumed that the temperature gradient close to the wellbore was equal to zero and the temperature at the far field remained at its initial value. The initial effective stress is equal to 3 MPa in the vertical direction and 1.5 MPa in the horizontal direction. The pressure and temperature remain constant at the far-end boundary, assuming depressurization close to the well has little impact on the far-end boundary. The values of the material properties, initial conditions, and boundary conditions are listed in Table 4.

Depressurization leads to compaction of the sediment layer due to the increase in mean effective stress. The rates of water and gas flow become faster due to the increase in pressure difference during the depressurization process. The temperature initially decreases due to hydrate dissociation, and then increases due to the heat convection and heat conduction occurring between the far-end higher temperature region and the dissociation region.

Fig. 18a shows the change in hydrate saturation during depressurization. Hydrate dissociation results in a decrease in hydrate saturation near the wellbore. The effective stresses increase with the drop in pore pressure. In addition, hydrate dissociation affects the mechanical behavior leading to stress relaxation. Fig. 18b shows that the mean effective stress increases as pore pressure decreases. However, after the hydrate dissociates, it falls because hydrate dissociation induces stress relaxation. Fig. 18c shows that deviator stress increases. This is due to the difference between the gradient of pore water pressure in the vertical direction and that in the radial direction. Stress is concentrated near the borehole. Fig. 18c also shows the stress relaxation that occurs by hydrate dissociation. An increase in mean effective stress results in formation compaction of the layers (Fig. 18d). In the no dissociation zone, the volumetric strain of the layer with hydrate is smaller than that of the layer without hydrate because the hydrate layer has higher stiffness. Fig. 18e shows that the temperature falls when hydrate dissociates, reflecting the endothermic process. The temperature then increases due to heat convection in which hot water and gas from the

Table 4 Model parameters

Parameter	Description
B_w (GPa)	2
B_g	p_g
p_0 (kPa)	10
n_1, n_2, n_3	0.8, 0.5, 0.5
K (m^2)	10^{-13}
N	5
K_{d0} (mol/(m^2·Pa·s))	1.24×10^5
ΔE_d (J/mol)	−78 300
K_{Ts} (W/(m·K))	3.92
ρ_s (kg/m^3)	2800
ρ_w (kg/m^3)	1000
M	0.3
p_{cs0} (MPa)	4.5
M	1.35
m	4
m_2 (MPa)	200
γ	0.85
λ	0.1
κ	0.006
K_{Tw} (W/(m·K))	0.556
K_{Tg} (W/(m·K))	0.0335
K_{Th} (W/(m·K))	0.394
β_w (K^{-1})	$13.41T$–3717
β_g (K^{-1})	$1/T$
β_h (K^{-1})	4.6×10^{-4}
c_s (J/(g·K))	0.8
c_w (J/(g·K))	$4.02+0.000\,577T$
c_g (J/(g·K))	$1.24+0.003\,13T$
c_h (J/(g·K))	2.01
N_h	6
P_{eq}	$e^{39.08-8520/T}$
ρ_h (kg/m^3)	800
χ_0	1
a	20
b	1
c	0.1
d	1
u	30
α	1

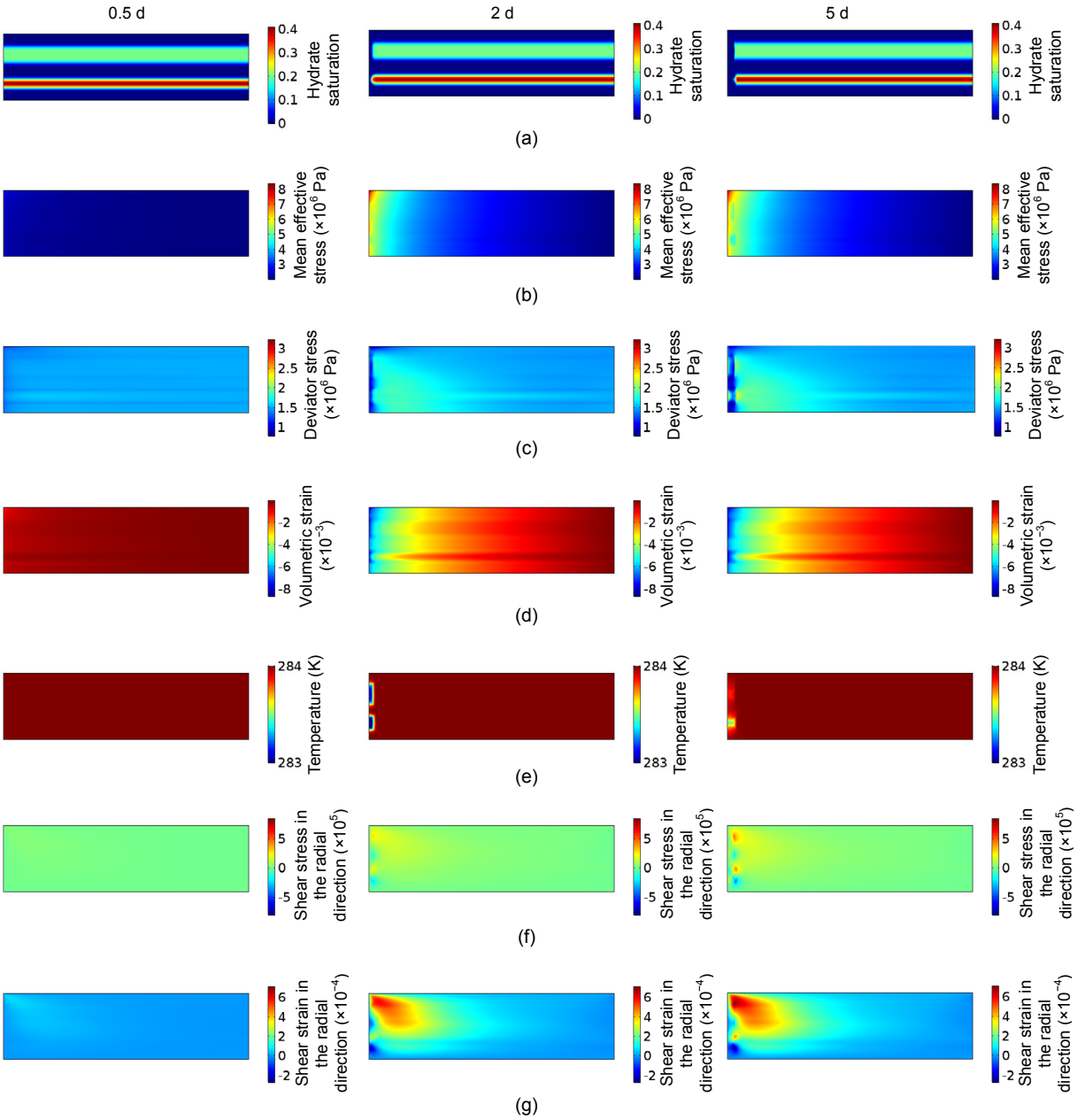

Fig. 18 Change of each variable with hydrate extraction under t=0.5 d, 2 d, and 5 d

(a) Hydrate saturation; (b) Mean effective stress; (c) Deviator stress; (d) Volumetric strain; (e) Temperature; (f) Shear stress in the radial direction; (g) Shear strain in the radial direction

far-end high temperature areas flow into the zone of lower temperature. Because hydrate occupies the pore space before dissociation, when it dissociates, more pore space becomes available for water and gas to flow through. Hence, the water permeability increases during hydrate dissociation.

Heat convection is an important behavior for the heterogeneous layers. The permeability in the hydrate layer where hydrate has dissociated is much greater than that in the layer without hydrate. The pressure gradient drives hot water and gas flow into the hydrate dissociated layer from the sediment layer without hydrate, prohibiting the temperature drop due to hydrate dissociation and boosting hydrate dissociation compared to the case of homogeneous layers. Due to the difference in the stiffness and strength of

the different layers, stress distribution is not uniform in the whole model, leading to a large stress gradient at the surface between the layers with and without hydrate. Shear stress increases in the interface (Fig. 18f), because the enhanced stiffness of the sediments due to the bonded structure formed by hydrates makes the deformation of the hydrate layer smaller than that of the layer without hydrate when the same loads are applied. Local shear strain exists in the interface and local shear stress is concentrated near the dissociation zone (Fig. 18g).

8 Conclusions

In this paper, we describe a mathematical framework based on the basic physical balance laws for porous media. Combining some auxiliary relationships, a fully coupled thermo-hydro-chemo-mechanical numerical model was implemented in COMSOL Multiphysics® to simulate the behavior of MHBS during methane gas extraction from hydrate bearing sediments by the depressurization method. The assumptions made for the implementation were presented. A thermodynamics-based constitutive model was implemented in COMSOL using its external material module to simulate the complicated mechanical behavior of MHBS. The accuracy of the model was verified by carefully comparing the simulated results with some triaxial test data available in the literature. The accuracy of the fully coupled THMC model without the mechanical part was validated by the gas production test data provided by Masuda et al. (1999). The performance of the code was similar to that of other simulators reported in the past.

The effect of full coupling compared with semi-coupling was investigated by simulating methane gas extraction by the depressurization method. Results showed that the changes in pressure, temperature, and hydrate saturation in the semi-coupled model were faster than those in the fully coupled model. The main reason for the difference was due to the volume change deformation, which influences the water and gas permeability and prolongs the pore pressure equalization diffusion process.

A case study of gas extraction from a heterogeneous hydrate layer system by depressurization was analyzed using the fully coupled model. Compared with a homogeneous model, a continuous heat supply from the layer without hydrate prohibited the temperature drop in the hydrate-dissociated layer due to hydrate dissociation, guaranteeing continuous gas production. Different mechanical properties of the different layers resulted in local shear stress and strain found at the interface between the hydrate layer and the layer without hydrate.

References

Ahmadi G, Ji C, Smith DH, 2004. Numerical solution for natural gas production from methane hydrate dissociation. *Journal of Petroleum Science and Engineering*, 41(4):269-285. https://doi.org/10.1016/j.profnurs.2003.09.004

Bishop AW, 1959. The principle of effective stress. *Teknik Ukeblad*, 39:859-863.

Borowski WS, Paul CK, 1997. The gas hydrate detection problem: recognition of shallow-subbottom gas hazards in deep-water areas. Offshore Technology Conference. https://doi.org/10.4043/8297-MS

COMSOL, 2017. Reference Manual Version 5.3. COMSOL Corporation, Stockholm, Sweden.

Gens A, 1996. Constitutive modelling: application to compacted soils. Proceedings of the 1st International Conference on Unsaturated Soils, p.1179-1200.

Hannegan D, Todd RJ, Pritchard DM, et al., 2004. MPD-uniquely applicable to methane hydrate drilling. SPE/IADC Underbalanced Technology Conference and Exhibition. https://doi.org/10.2118/91560-MS

Hyodo M, Kajiyama S, Yoshimoto N, et al., 2013a. Triaxial behaviour of methane hydrate bearing sand. Proceedings of the 10th ISOPE Ocean Mining and Gas Hydrates Symposium.

Hyodo M, Li YH, Yoneda J, et al., 2013b. Mechanical behavior of gas-saturated methane hydrate-bearing sediments. *Journal of Geophysical Research: Solid Earth*, 118(10):5185-5194. https://doi.org/10.1002/2013JB010233

Hyodo M, Li YH, Yoneda J, et al., 2014. Effects of dissociation on the shear strength and deformation behavior of methane hydrate-bearing sediments. *Marine and Petroleum Geology*, 51:52-62. https://doi.org/10.1016/j.marpetgeo.2013.11.015

Jommi C, di Prisco C, 1994. Un semplice approccio teorico per la modellazione del comportamento meccanico dei terreni granulari parzialmente saturi. Conference Il Ruolo dei Fluidi nei Problemi di Ingegneria Geotecnica, p.167-188 (in Italian).

Kakumoto M, Tenma N, Sakamoto Y, et al., 2011a. Development of the geo-mechanical simulation code COTHMA. Proceedings of the 9th ISOPE Ocean Mining

Symposium.

Kakumoto M, Yoneda J, Miyazaki K, et al., 2011b. Preliminary study on well integrity during gas production from methane hydrate sediments. Proceedings of the International Symposium on Earth and Technology.

Kamath VA, 1998. A perspective on gas production from hydrates. JNOC's Methane Hydrate International Symposium, p.20-22.

Kayen RE, Lee HJ, 1993. Slope stability in regions of sea-floor gas hydrate: Beaufort Sea continental slope. US Geological Survey Bulletin, USA, p.97-103.

Khalili N, Khabbaz MH, 1998. A unique relationship for χ for the determination of the shear strength of unsaturated soils. *Geotechnique*, 48(5):681-687. https://doi.org/10.1680/geot.1998.48.5.681

Kim HC, Bishnoi PR, Heidemann RA, et al., 1987. Kinetics of methane hydrate decomposition. *Chemical Engineering Science*, 42(7):1645-1653. https://doi.org/10.1016/0009-2509(87)80169-0

Kim J, Moridis G, Yang D, et al., 2012. Numerical studies on two-way coupled fluid flow and geomechanics in hydrate deposits. *SPE Journal*, 17(2):485-501. https://doi.org/10.2118/141304-PA

Kimoto S, Oka F, Fushita T, et al., 2007. A chemo-thermo-mechanically coupled numerical simulation of the subsurface ground deformations due to methane hydrate dissociation. *Computers and Geotechnics*, 34(4):216-228. https://doi.org/10.1016/j.compgeo.2007.02.006

Klar A, Soga K, Ng MYA, 2010. Coupled deformation–flow analysis for methane hydrate extraction. *Geotechnique*, 60(10):765-776. https://doi.org/10.1680/geot.9.P.079-3799

Kowalsky MB, Moridis GJ, 2007. Comparison of kinetic and equilibrium reaction models in simulating gas hydrate behavior in porous media. *Energy Conversion and Management*, 48(6):1850-1863. https://doi.org/10.1016/j.enconman.2007.01.017

Li YH, Liu WG, Song YC, et al., 2016a. Creep behaviors of methane hydrate coexisting with ice. *Journal of Natural Gas Science and Engineering*, 33:347-354. https://doi.org/10.1016/j.jngse.2016.05.042

Li YH, Liu WG, Zhu YM, et al., 2016b. Mechanical behaviors of permafrost-associated methane hydrate-bearing sediments under different mining methods. *Applied Energy*, 162:1627-1632. https://doi.org/10.1016/j.apenergy.2015.04.065

Masuda Y, Fujinaga Y, Naganawa S, et al., 1999. Modeling and experimental studies on dissociation of methane gas hydrates in Berea sandstone cores. Proceedings of the 3rd International Gas Hydrate Conference.

Masui A, Haneda H, Ogata Y, et al., 2006. Triaxial compression test on submarine sediment containing methane hydrate in deep sea off the coast off Japan. Proceedings of the 41st Annual Conference, Japanese Geotechnical Society.

Masui A, Haneda H, Ogata Y, et al., 2007. Compaction behavior of Toyoura sand during methane hydrate dissociation. Proceedings of the 7th ISOPE Ocean Mining Symposium.

McIver RD, 1982. Role of naturally occurring gas hydrates in sediment transport. *AAPG Bulletin*, 66(6):789-792.

Minagawa H, Nishikawa Y, Ikeda I, et al., 2008. Characterization of sand sediment by pore size distribution and permeability using proton nuclear magnetic resonance measurement. *Journal of Geophysical Research: Solid Earth*, 113(B7):B07210. https://doi.org/10.1029/2007JB005403

Moridis GJ, Collett TS, Dallimore SR, et al., 2004. Numerical studies of gas production from several CH_4 hydrate zones at the Mallik site, Mackenzie Delta, Canada. *Journal of Petroleum Science and Engineering*, 43(3-4):219-238. https://doi.org/10.1016/j.petrol.2004.02.015

Paull CK, Ussler W, Dallimore SR, et al., 2007. Origin of pingo-like features on the Beaufort Sea shelf and their possible relationship to decomposing methane gas hydrates. *Geophysical Research Letters*, 34(1):L01603. https://doi.org/10.1029/2006GL027977

Ruppel C, 2011. Methane Hydrates and the Future of Natural Gas. MITEI Natural Gas Report, Supplementary Paper on Methane Hydrates, p.25.

Sakamoto Y, Komai T, Miyazaki K, et al., 2010. Laboratory-scale experiments of the methane hydrate dissociation process in a porous media and numerical study for the estimation of permeability in methane hydrate reservoir. *Journal of Thermodynamics*, 2010:452326. https://doi.org/10.1155/2010/452326

Schrefler BA, 1984. The Finite Element Method in Soil Consolidation. MS Thesis, University College of Swansea, Swansea, UK.

Song YC, Yu F, Li YH, et al., 2010. Mechanical property of artificial methane hydrate under triaxial compression. *Journal of Natural Gas Chemistry*, 19(3):246-250. https://doi.org/10.1016/S1003-9953(09)60073-6

Song YC, Wang XJ, Yang MJ, et al., 2013. Study of selected factors affecting hydrate-based carbon dioxide separation from simulated fuel gas in porous media. *Energy & Fuels*, 27(6):3341-3348. https://doi.org/10.1021/ef400257a

Song YC, Cheng CX, Zhao JF, et al., 2015. Evaluation of gas production from methane hydrates using depressurization, thermal stimulation and combined methods. *Applied Energy*, 145:265-277. https://doi.org/10.1016/j.apenergy.2015.02.040

Sun X, Guo XX, Shao LT, et al., 2015. A thermodynamics-based critical state constitutive model for methane hydrate bearing sediment. *Journal of Natural Gas Science and Engineering*, 27:1024-1034. https://doi.org/10.1016/j.jngse.2015.09.048

Taylor DW, 1948. Fundamentals of Soil Mechanics. Chapman and Hall, London, UK.

Uchida S, 2013. Numerical Investigation of Geomechanical Behaviour of Hydrate-bearing Sediments. MS Thesis,

University of Cambridge, Cambridge, UK.

Uchida S, Soga K, Yamamoto K, 2012. Critical state soil constitutive model for methane hydrate soil. *Journal of Geophysical Research: Solid Earth*, 117(B3):B03209. https://doi.org/10.1029/2011JB008661

Uchida S, Xie XG, Leung YF, 2016a. Role of critical state framework in understanding geomechanical behavior of methane hydrate-bearing sediments. *Journal of Geophysical Research: Solid Earth*, 121(8):5580-5595. https://doi.org/10.1002/2016JB012967

Uchida S, Deusner C, Klar A, et al., 2016b. Thermo-hydro-chemo-mechanical formulation for CH_4-CO_2 hydrate conversion based on hydrate formation and dissociation in hydrate-bearing sediments. Geo-Chicago 2016, p.235-244. https://doi.org/10.1061/9780784480137.024

van Genuchten MT, 1980. A closed-form equation for predicting the hydraulic conductivity of unsaturated soils. *Soil Science Society of America Journal*, 44(5):892-898. https://doi.org/10.2136/sssaj1980.03615995004400050002x

Wilder JW, Moridis GJ, Wilson SJ, et al., 2008. An international effort to compare gas hydrate reservoir simulators. Proceedings of the 6th International Conference on Gas Hydrates (ICGH 2008).

Yang MJ, Song YC, Jiang LL, et al., 2014. Hydrate-based technology for CO_2 capture from fossil fuel power plants. *Applied Energy*, 116:26-40. https://doi.org/10.1016/j.apenergy.2013.11.031

Zhao JF, Yao L, Song YC, et al., 2011. In situ observations by magnetic resonance imaging for formation and dissociation of tetrahydrofuran hydrate in porous media. *Magnetic Resonance Imaging*, 29(2):281-288. https://doi.org/10.1016/j.mri.2010.08.012

Zhao JF, Yu T, Song YC, et al., 2013. Numerical simulation of gas production from hydrate deposits using a single vertical well by depressurization in the Qilian Mountain permafrost, Qinghai-Tibet Plateau, China. *Energy*, 52:308-319. https://doi.org/10.1016/j.energy.2013.01.066

Zhao JF, Liu D, Yang MJ, et al., 2014. Analysis of heat transfer effects on gas production from methane hydrate by depressurization. *International Journal of Heat and Mass Transfe*r, 77:529-541. https://doi.org/10.1016/j.ijheatmasstransfer.2014.05.034

Zhao JF, Zhu ZH, Song YC, et al., 2015. Analyzing the process of gas production for natural gas hydrate using depressurization. *Applied Energy*, 142:125-134. https://doi.org/10.1016/j.apenergy.2014.12.071

中文概要

题　目：基于 COMSOL Multiphysics 天然气水合物沉积物热-水-力-化多场耦合模型研究

目　的：水合物沉积物开采过程是一个热-水-力-化多场耦合过程，该过程包含了不同土层间的热对流、压缩引起的局部变形以及胶结结构破坏引起的应力松弛。不适当的开采会引起出砂、塌孔等破坏问题。本文旨在建立天然气水合物沉积物多场耦合计算模型，以量化由开采引起的地质灾害风险。

创新点：1. 通过 COMSOL Multiphysics 实现水合物开采过程多场耦合有限元控制方程的计算；2. 建立的模型考虑变形-渗流双向全耦合过程。

方　法：1. 通过理论推导，给出开采天然气水合物过程模拟的控制方程；采用偏微分方程模块实现除力学之外其他物理场的耦合计算；采用结构力学模块实现变形计算。2. 通过与试验数据进行比较验证模型的可靠性。3. 通过对比全耦合模型与半耦合模型，分析双向耦合对水合物开采过程中沉积物物理力学行为的影响。

结　论：1. 所建立模型能够精确模拟水合物开采过程中沉积物的物理力学行为。2. 当考虑压缩对渗流的影响时，由于孔隙率的降低，计算得到的水合物分解速度要小于不考虑该影响时的速度。3. 由于存在层间对流效应，非均质模型计算得到的水合物分解速度要快于均质模型。

关键词：水合物沉积物；多场耦合模型；COMSOL；产气